Terrain Parameter Estimation and Traversability Assessment for Mobile Robots

by

Shinwoo Kang

B.S., Mechanical Engineering (2001)
Seoul National University

Submitted to the Department of Mechanical Engineering
in Partial Fulfillment of the Requirements for the Degree of

Master of Science in Mechanical Engineering

at the

Massachusetts Institute of Technology

May 2003

Signature of Author .....
Department of Mechanical Engineering
May 12, 2003

Certified by .....
Steven Dubowsky
Professor of Mechanical Engineering
Thesis Supervisor

Accepted by .....
Ain A. Sonin
Chairman, Department Committee on Graduate Students

Terrain Parameter Estimation and Traversability Assessment for Mobile Robots

by
Shinwoo Kang

Submitted to the Department of Mechanical Engineering
on May 12, 2003, in Partial Fulfillment of the
Requirements for the Degree of
Master of Science in Mechanical Engineering

Abstract

The estimation of terrain characteristics is an important missions of Martian exploration rovers. Since only limited resources and human supervision are available, efficient and autonomous method of estimation are required. In this thesis, an on-line estimation method of two important terrain parameters, cohesion and internal friction angle, is developed. The method uses on-board rover sensors and is computationally efficient. Terrain parameter estimation is of scientific interest, and can also be useful in predicting rover mobility on rough-terrain. A method to estimate traversability of a rover on deformable terrain using on-board sensors is presented. Simulation and experimental results show that the proposed methods can accurately and efficiently estimate traversability of deformable terrain.

Thesis Supervisor: Steven Dubowsky

Title: Professor of Mechanical Engineering

Acknowledgments

Thanks for all the people who helped me during the two years in MIT: Prof. Dubowsky and Karl for their advice on my research, all the FSRL people, my parents, and my friends.

This work was supported by the NASA Jet Propulsion Laboratory. The Author would like to acknowledge the support and assistance of Dr. Rich Volpe and Dr. Paul Schenker at JPL.

Contents

List of Figures

List of Tables

Chapter 1: Introduction

1.1 Motivation

Space exploration has been a great interest for mankind. The U.S. government has expended considerable effort to explore nearby planets, especially Mars. The first Mars exploration craft, the Viking lander, successfully landed on Mars on July 20, 1976 (see Figure 1.1). The Viking lander performed several experiments to measure terrain parameters, especially cohesion (c) and internal friction angle (φ) [1]. The experimental data were sent back to earth with images of the Martian surface and then analyzed to determine the values of c and φ.

On July 4, 1997, the second Mars exploration, the Mars Pathfinder mission landed the Sojourner on Mars (see Figure 1.2). The mission objectives of Sojourner included investigations of the surface morphology and geology at submeter to hundred meter scale, the petrology and geochemistry of rocks and soils, the magnetic properties of dust, and soil mechanics and properties [2]. Sojourner did mechanical and chemical experiments on Martian soil to obtain the terrain properties c and φ. Sojourner sent all the experimental data to earth, where the analysis was done [3].

For a planetary exploration rover such as Sojourner, it is important to understand the nature of the terrain it is about to traverse to avoid wheel slip and excessive sinkage. Cohesion (c) and internal friction angle (φ) are arguably the most useful terrain parameters [4]. An efficient method of measuring terrain parameters would enlarge the rover capability to reach mission objectives while using saved resources. A method to use this terrain information for path-planning and safety assessment would be also helpful in achieving rover mission goals.

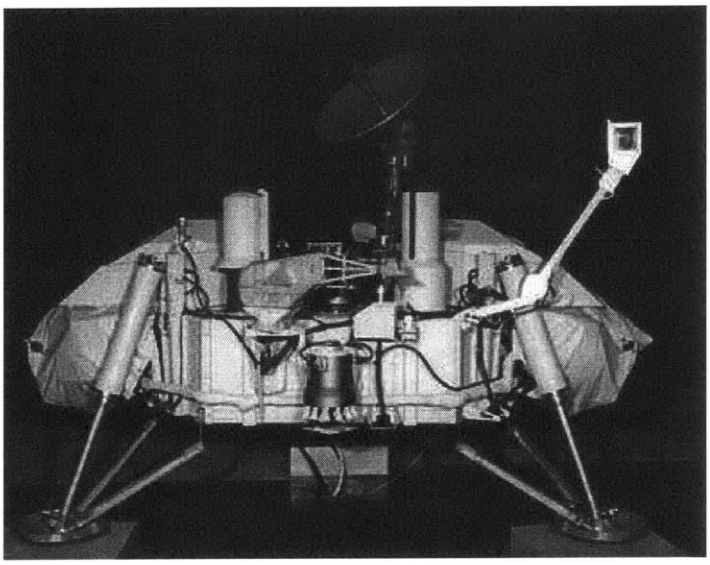

Figure 1.1 Viking Mars Lander (Mars Pathfinder website: http://mars.jpl.nasa.gov/MPF)

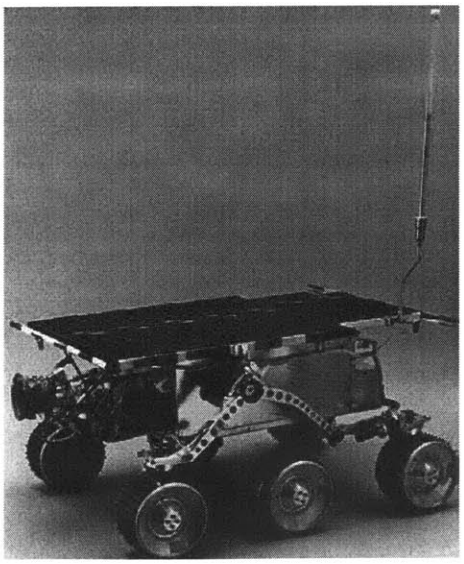

Figure 1.2 Sojourner Pathfinder rover (Mars Pathfinder website: http://mars.jpl.nasa.gov/MPF)

In planetary exploration missions, the amount of available power and time is restricted and thus effective use of them is indispensable. Effective experimental methods can save valuable power and time, which can enable other mission achievements. For the previous missions, terrain parameter estimations were performed either with special equipment (Viking lander's surface sampler) or by spending a significant amount of time on the experimental spot (Sojourner wheel spin experiment). All the experimental data had to be sent back to earth for analysis, which can take hours or days. Use of special equipment requires additional rover equipment capacity and power. Excessive time consumption on one task reduces rover working time for other tasks. A more efficient method of terrain parameter estimation will lead to completion of more mission goals and/or faster completion of tasks.

Information on terrain parameters not only has scientific interest, but is also useful for safe navigation of the rover. When the terrain is rough and deformable, it is possible for a rover to lose mobility and get trapped in the terrain. This loss of mobility causes mission failure and must be avoided. To avoid these situations, it is important to assess terrain traversability. Without considering the terrain characteristics, safe motion planning and control is difficult to achieve. A method to deal with this information will help in planning safe paths and controlling rover motion.

1.2 Related Research

1.2.1 Terrain Parameter Estimation

The most common terrain parameter estimation method is the one proposed by Bekker [5]. Bekker relates three terrain parameters $(k_c,\ k_\varphi$ and $n)$, to the dimensions of a rectangular plate (b), the sinkage (z) of the plate into the terrain, and the normal stress (σ) developed between the plate and terrain:

$$\sigma = \left(\frac{k_c}{b} + k_\varphi \right) \cdot z^n \tag{1.1}$$

Terrain parameters k_c, k_φ and n in Equation (1.1) can be determined by curve fitting on experimental data gathered by applying various weights on plates with different dimensions. Bekker developed an experimental apparatus called Bevameter to measure these terrain parameters (see Figure 1.3) [5].

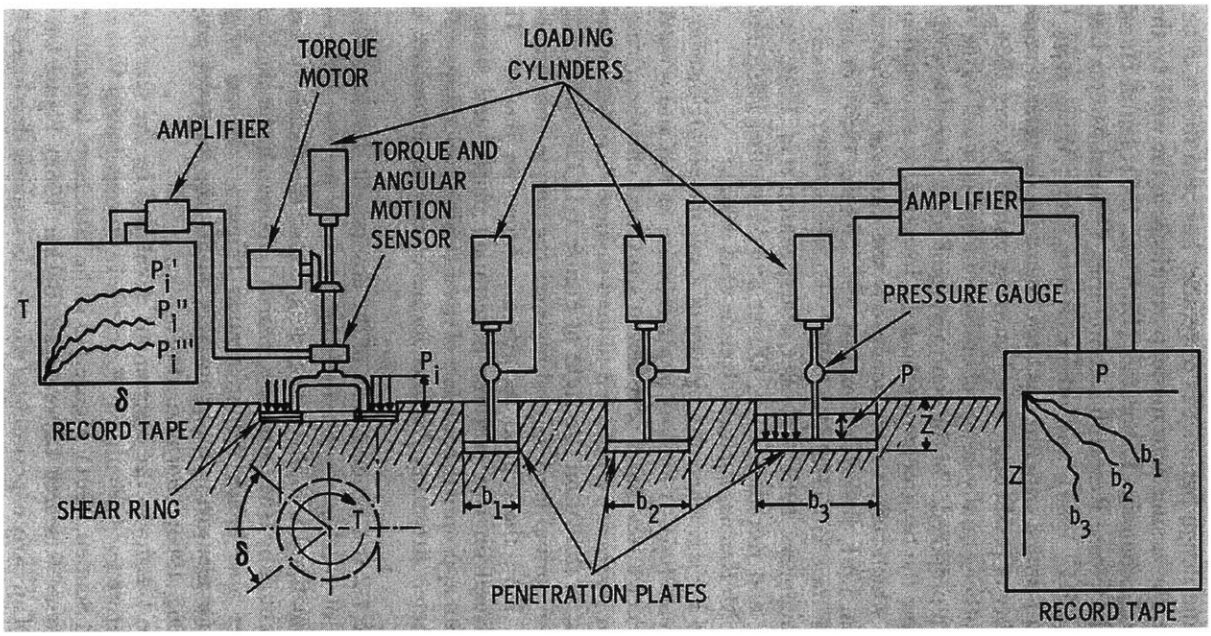

Figure 1.3 Schematic view of Bevameter ("Introduction to Terrain-Vehicle Systems" by M.G. Bekker)

When the plate moves horizontally, shear stress τ develops on the plate-terrain interface. The relationship between the normal stress and the shear stress can be described by an exponential function [6]:

$$\tau = (c + \sigma \tan\varphi)\left(1 - e^{-\frac{j}{K}}\right) \tag{1.2}$$

where

j: shear displacement, K: shear deformation modulus

The cohesion (c), internal friction angle (φ) and shear deformation modulus (K) can be measured by applying different normal stresses, measuring the associated shear stresses and displacements, and fitting the data according to these normal and shear stress relations (Equation 1.2). This method requires the Bevameter and this need of special equipment makes this method not practical for Mars exploration missions. Bekker's Equation (1.1) explains the normal stress distribution under a rectangular plate well, but it is not appropriate to be directly applied to a wheel-terrain interaction. Wong developed a method to estimate the stress distributions between a rigid wheel and deformable terrain (see Appendix C) [7].

The Viking landers used a surface sampler (a robotic arm) to measure the cohesion and internal friction angle of the Martian terrain (see Figure 1.4) [1]. The interaction forces of the surface sampler and terrain, and the size of a trench the surface sampler made were measured. All the data were sent back to earth to be analyzed off-line. A plowing model of a narrow blade was used to analyze the interaction forces [8]. This method can only be used for rovers with specially equipped robotic arms, which add weight and power requirement. Further, the rover must stop to perform experiments, which can take significant amount of time.

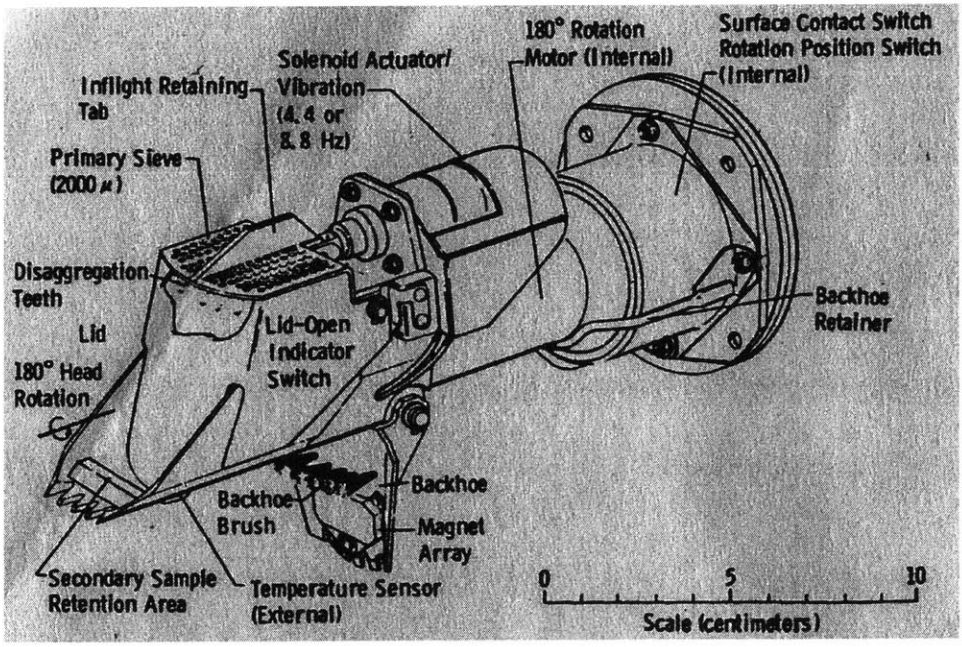

Figure 1.4 Drawing of Viking Lander's sampler arm
("A summary of Viking Sample-Trench Analysis for Angles of Internal Friction and Cohesions" by H.J. Moore)

Sojourner measured the cohesion and internal friction angle of the Martian terrain by using its wheel as the experimental tool. During the experiment, one wheel was commanded to rotate while others were held fixed. The wheel weight and shear force was derived from the measurement of the wheel torque and the bogie positions. The wheel sinkage was measured from the lander camera images of rover tracks, and the rover images of the wheel in the soil [4]. Table 1.1 shows detailed experimental steps Sojourner rover performed. Area of the wheel-terrain interface was derived from the sinkage. The weight and shear forces were assumed to be uniformly distributed on the wheel-terrain interface as normal and shear stresses. The Mohr-Coulomb equation of normal-shear stress (Equation 1.3) and least-square curve fitting were used to estimate c and φ. All the data were sent back to earth and the analysis was done off-line [3].

$$\tau = c + \sigma \tan\varphi$$
$$\tau: \text{shear stress} \quad \sigma: \text{normal stress} \qquad (1.3)$$
$$c: \text{cohesion} \quad \varphi: \text{internal friction angle}$$

Since the Sojourner method uses its wheel as a measuring instrument, it doesn't need any special tools. However, the rover must stop at the experiment location and do multiple sets of experiments.

Table 1.1 Generalized baseline soil mechanics experiment

Step	Description
1	Move to experiment site.
2	Acquire rear rover camera image of experiment area.
3	Rotate right rear wheel one turn forward in quarter turn steps.
4	Acquire rear rover camera image of wheel in excavation.
5	Acquire lander camera stereo-pair image of wheel in excavation.
6	move forward 20 cm.
7	Acquire rear rover camera image of excavation.
8	Rotate right front wheel one turn forward in quarter-turn steps with 0.0075 turns of the right center wheel backward after each quarter turn.
9	Align left front and two rear steering motors to push on right front.
10	Acquire right front rover camera image of experiment area.
11	Move forward 8 cm.
12	Acquire lander camera stereo-pair image of wheel in excavation.
13	Acquire lest front rover camera image of surface in front of right wheel.
14	Acquire right front rover camera image lf surface in front of right front wheel.
15	Move backward 8 cm.

Hong developed a method to measure internal friction angle (φ) of cohesionless soil by using a robotic arm (see Figure 1.5) [9]. A rectangular plate was attached to the robotic arm and used as a digging tool. By measuring the forces the arm stroke generated in the soil, the internal friction angle could be directly computed. To apply this method, a robotic arm which can sense all the forces it generates is needed and the soil must be cohesionless.

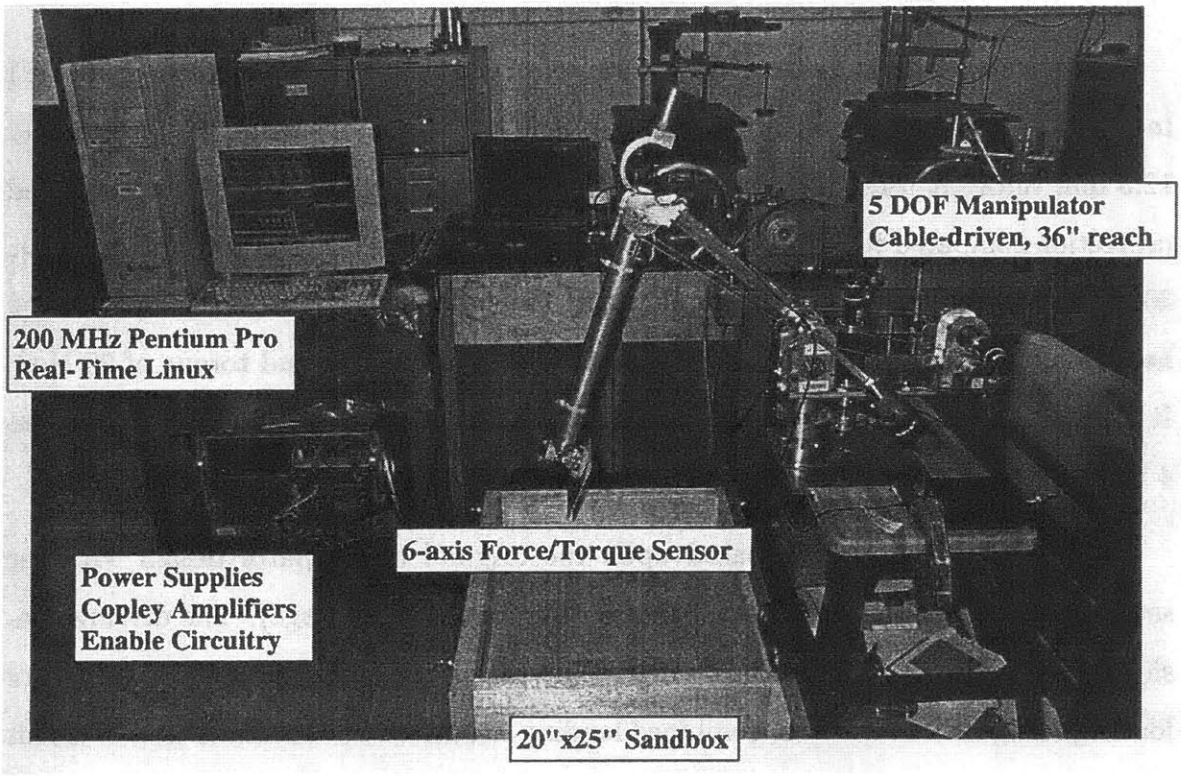

Figure 1.5 Robotic arm used in Hong's estimation experiment
("Modeling, Estimation, and Control of Robot-Soil Interactions" by W. Hong, Ph.D thesis at MIT)

The above four estimation methods need either dedicated experimental tools or long experimental time and many trials. For resource-restricted systems such as planetary exploration rovers, these requirements are very hard to achieve.

Iagnemma suggested a method to estimate terrain parameters c and φ using a rover wheel (see Appendix B) [17]. This method is computationally efficient and can accomplish on-line estimation. However, this method tends to yield error on high cohesion soils.

1.2.2 Traversability Assessment

Path planning of vehicles on rough terrain has been studied by many researchers. A few researchers have suggested methods to incorporate terrain information on path-planning methods [24].

Kelly and Stentz developed a navigation method which includes perception by vision, mapping, obstacle detection and avoidance, and goal seeking on rough terrain [11]. Terrain geometry such as slope, ravine and obstacles (trees or rocks) are detected by vision sensors (cameras) and considered in path-planning. The basic assumption on the terrain model is that the terrain is rigid, which is not true for off-road situations.

Davis developed a real-time terrain typing method for robots [12]. This method distinguishes vegetation, which is easy to pass over, from rigid obstacles, which should be avoided. The primary sensor for data-gathering is stereo vision.

Singh proposed and validated a method which could assess local and global traversability of terrain based on visual information [13]. Binocular stereo vision was used to sense outdoor terrain. Traversability of terrain was determined based on information on the terrain roughness, and the roll and pitch angle a rover would experience on that terrain.

Gennery researched a method of analyzing three-dimensional data obtained from stereo vision [14]. This method estimates height, slope and roughness of terrain and then computes a cost function of distance and traversability of the planned path. A parallel search algorithm is used to find out the path of optimum cost.

Howard and Seraji developed a fuzzy-logic based method to assess terrain traversability and path-plan using information on terrain roughness, slope, discontinuity, and texture [15, 22]. An intuitive and linguistic approach for expressing terrain characteristics was used to robustly accommodate the imprecision and uncertainty in the terrain measurements.

Iagnemma proposed a physics-based rough-terrain rover path-planning method that is computationally efficient and takes into account rover capability, terrain roughness, and uncertainty in the terrain model, robot model, sensor data, and rover path following error [16]. The terrain model used in this method was the rigid terrain with slope and geometric obstacles, without considering the terrain characteristics such as hardness, cohesion and friction.

None of these methods include the non-geometric terrain characteristics such as hardness, cohesion and friction in assessing terrain traversability. However, in case of deformable terrain, which is common on Martian surface, these parameters play an important role (see Figure 1.6) [23]. For example, on slippery terrain such as wet clay or loose sand, it is possible for a vehicle to lose traction and become immobilized. In planetary rover missions, this loss of mobility means mission failure and must be avoided in any circumstance. Thus, to plan a safe path on rough and deformable terrain, terrain characteristics must be considered.

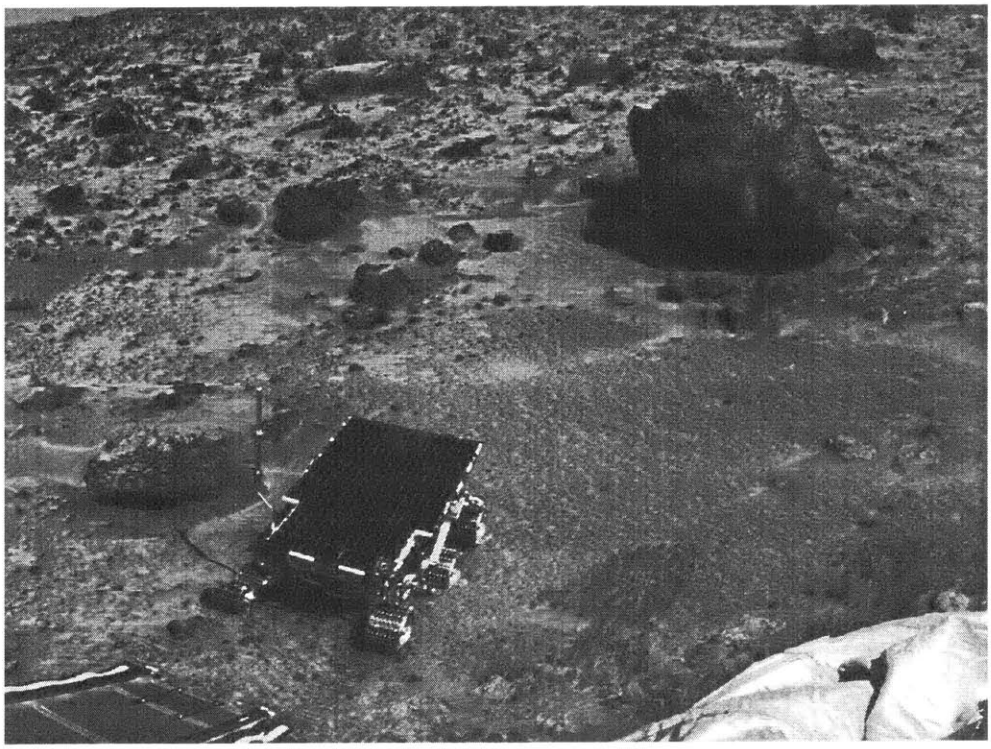

Figure 1.6 Sojourner landing site on Mars. A rover should traverse rough and deformable environment. (Mars Pathfinder website: http://mars.jpl.nasa.gov/MPF)

1.3 Purpose of Thesis

The purpose of this thesis is twofold:

1. Develop a terrain parameter estimation method which uses on-board rover sensors, minimal power and computation time, and is efficient enough for on-line estimation.
2. Develop a method to assess terrain traversability from simple rover sensors. With an understanding of terrain traversability, path planning and control methods can be adapted to be more efficient.

1.4 Outline of Thesis

This thesis is composed of four chapters and four appendices. This chapter is the introduction and overview of the work.

In Chapter 2, a brief review of traditional terrain parameter estimation will be presented. Then a newly proposed method will be discussed and verified with simulation and experimental results.

In Chapter 3, a method for assessing terrain traversability based on wheel sinkage and torque will be discussed. The importance of traversability assessment will be briefly stated and the proposed method will be verified with simulation and experimental results.

Chapter 4 concludes this thesis and briefly talks about the limits of this work and related future research goals.

The appendices of this thesis cover:

A: Basic terramechanics

B: Terrain parameter estimation methods

C: Wheel-terrain interaction models

D: Shear deformation modulus estimation

Chapter 2: Terrain Characterization

2.1 Introduction

Terrain parameter estimation has been of great interest for planetary exploration researchers. Viking landers [1] and Sojourner Pathfinder [3] on Mars have performed many experiments to estimate properties of Martian surface terrain such as cohesion (c) and internal friction angle (φ). These experiments were done with special equipment (a surface sampler) and/or by stopping at the experiment spot and devoting substantial time to perform multiple experiments. Estimation results from these experiments showed good matches to expected values, and resulted in meaningful science information about the Martian surface terrain. However, the need of special equipment or long experimental time are hard to fulfill in exploration missions where available resources are very restricted. Here, a new method for parameter estimation which uses a rover wheel as experimental equipment and requires small computation and experimentation time is developed and verified.

2.2 Terrain Parameter Estimation

Iagnemma [17] suggested a method for on-line estimation of terrain parameters using a wheel. Wong's model of wheel-terrain interaction [7] is used in his work. Figure 2.1 shows a schematic diagram of parameters on the wheel-terrain interaction. This method needs multiple sensor data points for the wheel weight, torque, sinkage and slip ratio in estimating stress distribution on the wheel-terrain interface. The estimated stress distributions are manipulated to estimate terrain parameters. A least-square method is used in estimating the cohesion and internal friction angle of terrain the rover traverses. The heart of this method is the assumption of a linear normal and shear stress profile at the wheel-terrain interface. The simplified linear stress distribution approximates the nonlinear distribution closely on low-cohesion soils (Figure 2.2 a). However, the approximation shows deviance for cohesive soils. It can be shown that for the high cohesion cases, there is error when the contact angle is small (Figure 2.2 b). This leads to error in parameter estimation. When Iagnemma's estimation algorithm is used in prediction of parameters for cohesive soil, it can produce larger cohesion and smaller internal friction angle (see Figure 2.3). To compensate for this propensity, a modified approximation method which can take high cohesions into account is needed.

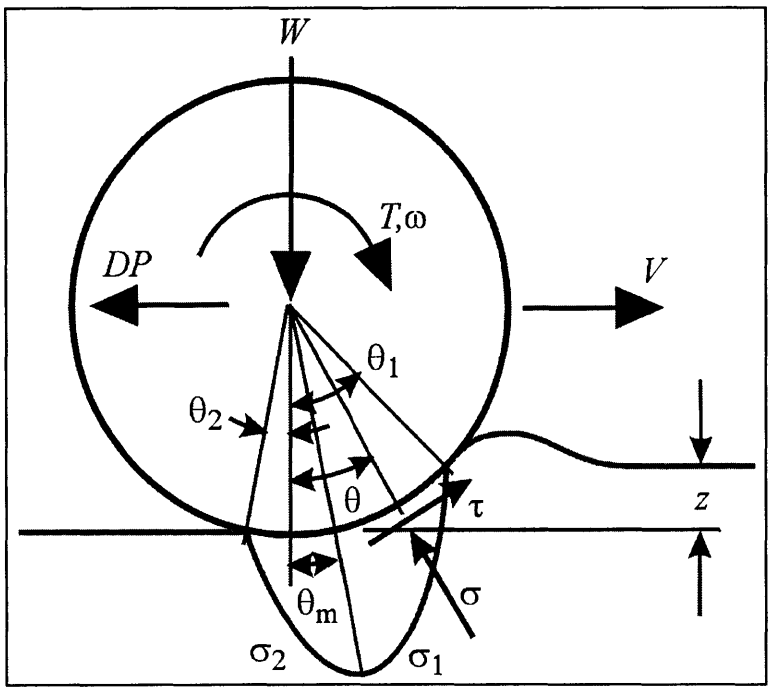

Figure 2.1 Wheel-terrain interaction model
("Multi-Sensor Terrain Estimation for Planetary Rovers" by K. Iagnemma [17])

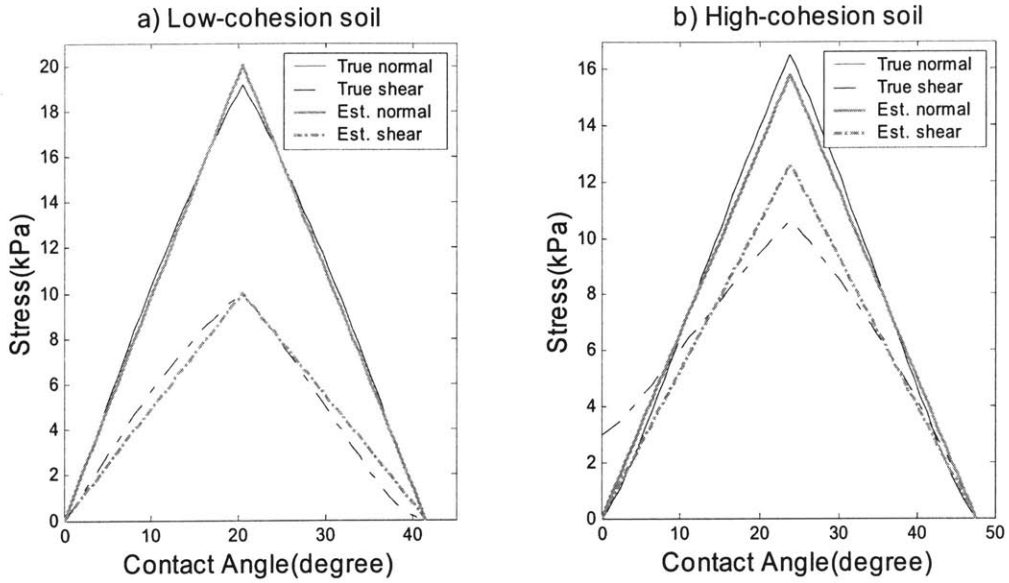

Figure 2.2 Stress distributions along wheel rim – linear approximation.

In Figure b), estimated shear stress shows deviance from true shear stress at small contact angle.

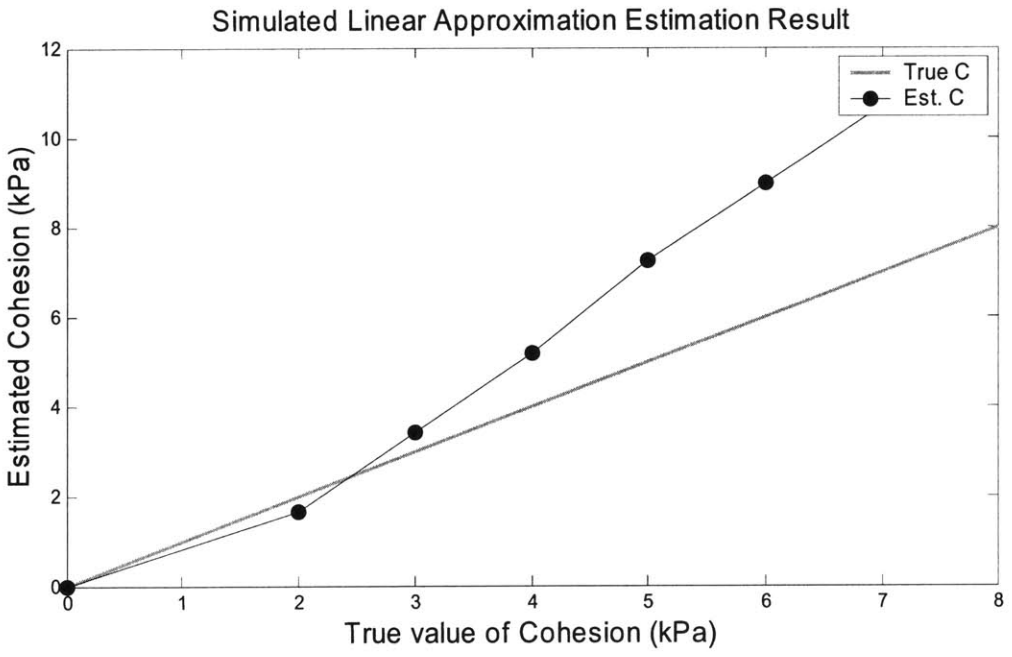

Figure 2.3 Simulated linear approximation estimation result: estimated c is bigger than true value.

To accommodate the values of shear stress at small contact angles, a new method of linear approximation can be expressed as follow:

$$\sigma_1(\theta)=\frac{\theta_1-\theta}{\theta_1-\theta_m}\sigma_m \quad (\theta_m \le \theta \le \theta_1), \qquad \sigma_2(\theta)=\frac{\theta}{\theta_m}\sigma_m \quad (0 \le \theta \le \theta_m)$$

$$\tau_1(\theta)=\frac{\theta_1-\theta}{\theta_1-\theta_m}\tau_m \quad (\theta_m \le \theta \le \theta_1), \qquad \tau_2(\theta)=\tau_{offset}+(\tau_m-\tau_{offset})\frac{\theta}{\theta_m} \quad (0 \le \theta \le \theta_m) \tag{2.1}$$

By introducing an offset term at $\theta = 0$, the estimated stress profile can better approximate the actual stress distribution. Figure 2.4 shows that this modified linear approximation can closely follow the nonlinear stress distributions on both low- and high-cohesion soils.

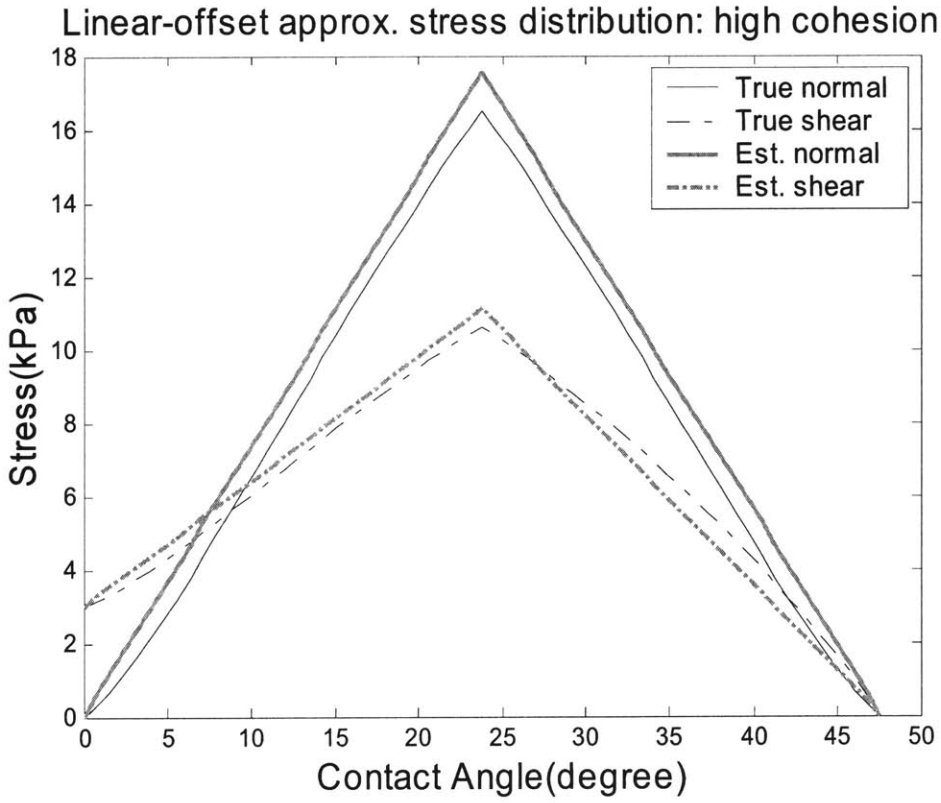

Figure 2.4 Stress distribution along wheel rim – linear-offset approximation.
Approximated stress distributions follow true stress distributions well on most contact angle.

This implies that linear approximation can thus be used in a parameter estimation algorithm. To estimate terrain parameters c and φ, the stress distribution σ and τ in Equation 2.1 must be estimated first.

Equation 2.1 has four unknown parameters: θ_m, σ_m, τ_m, τ_{offset}. Force balance equations on wheel weight W and wheel torque T can be written as:

$$T = r^2 b\left[\int_0^{\theta_m} \tau_2(\theta)\,d\theta + \int_{\theta_m}^{\theta_1} \tau_1(\theta)\,d\theta\right] = r^2 b\left(\frac{\theta_1}{2}\tau_m + \frac{\theta_m}{2}\tau_{offset}\right) \tag{2.2}$$

$$\begin{aligned} W &= rb\left[\int_0^{\theta_m}\left(\sigma_2(\theta)\cos\theta + \tau_2(\theta)\sin\theta\right)d\theta + \int_{\theta_m}^{\theta_1}\left(\sigma_1(\theta)\cos\theta + \tau_1(\theta)\sin\theta\right)d\theta\right] \\ &= rb\left(\frac{\cos\theta_m}{\theta_m} - \frac{\cos\theta_1 - \cos\theta_m}{\theta_1 - \theta_m} - \frac{1}{\theta_m}\right)\sigma_m \\ &\quad + rb\left(\frac{\sin\theta_m}{\theta_m} - \frac{\sin\theta_1 - \sin\theta_m}{\theta_1 - \theta_m}\right)\tau_m + rb\left(\cos\theta_m - \frac{\sin\theta_m}{\theta_m} + \theta_m\right)\tau_{offset} \end{aligned} \tag{2.3}$$

The equation describing the relationship between the normal and shear stress also provides valuable information (Equation 2.4). Two more equations are obtained from setting $\theta = 0$ and $\theta = \theta_m$ on the normal-shear stress relation (Equation 2.5, 2.6). A further assumption that $\theta_m = \frac{\theta_1}{2}$ with known K establishes another piece of information (Equation 2.8). Shear deformation modulus can be estimated from the measured values of the wheel weight, torque, sinkage and slip ratio (see Appendix D).

$$\tau(\theta) = \left(c + \sigma(\theta)\tan\phi\right)\left(1 - e^{-\frac{r}{K}(\theta_1 - \theta - (1-i)(\sin\theta_1 - \sin\theta))}\right) \tag{2.4}$$

$$\tau_m = \tau(\theta_m) = \left(c + \sigma_m \tan\phi\right)\left(1 - e^{-\frac{r}{K}(\theta_1 - \theta_m - (1-i)(\sin\theta_1 - \sin\theta_m))}\right) = \left(c + \sigma_m \tan\phi\right)A \tag{2.5}$$

$$\tau_{offset} = \tau(0) = c\left(1 - e^{-\frac{r}{K}(\theta_1 - (1-i)\sin\theta_1)}\right) = cB \tag{2.6}$$

where

$$A = 1 - e^{-\frac{r}{K}(\theta_1 - \theta_m - (1-i)(\sin\theta_1 - \sin\theta_m))}, \quad B = 1 - e^{-\frac{r}{K}(\theta_1 - (1-i)\sin\theta_1)} \tag{2.7}$$

$$\theta_m = \frac{\theta_1}{2} \tag{2.8}$$

K: known in advance

Equations (2.2), (2.3), (2.5), (2.6) and (2.8) represent 5 equations in 6 unknown parameters (θ_m, σ_m, τ_m, τ_{off}, c, φ). By manipulating these five equations and six unknown parameters, one equation with two unknowns can be derived. As the most interesting parameters are cohesion c and internal friction angle φ, the equation can be rewritten in terms of c and φ:

$$M_1 c\tan\varphi + M_2 c + M_3\tan\varphi = M_4 \tag{2.9}$$

where

$$M_1 = -\frac{\left(1 - \frac{4}{\theta_1}\sin\frac{\theta_1}{2} + \frac{\sin\theta_1}{\theta_1}\right)B}{\frac{2}{\theta_1}\left(2\cos\frac{\theta_1}{2} - \cos\theta_1 - 1\right)\left(1 + \frac{B}{2A}\right)}, \quad M_2 = 1$$

$$M_3 = \frac{\left(\frac{W}{rb} - \left(2\sin\frac{\theta_1}{2} - \sin\theta_1\right)\frac{4T}{\theta_1^2 r^2 b}\right)}{\frac{2}{\theta_1}\left(2\cos\frac{\theta_1}{2} - \cos\theta_1 - 1\right)\left(1 + \frac{B}{2A}\right)}, \quad M_4 = \frac{2T}{\theta_1 r^2 bA\left(1 + \frac{B}{2A}\right)} \tag{2.10}$$

For most soil types, wheel slip ratios and sinkage conditions, the magnitude of M_1 is small compared with other coefficients in Equation 2.10. Figure 2.5 shows the magnitude of each coefficient on a representative terrain and operating conditions. It can be seen that the first term $M_1 c\tan\varphi$ is less than 10% of the second smallest term $M_2 c = c$ and thus can be ignored without loss of generality. Equation 2.9 therefore becomes a single linear form of Equation 2.11 (M_3 and M_4 are as defined in Equation 2.10):

$$c + M_3 * \tan\varphi = M_4 \tag{2.11}$$

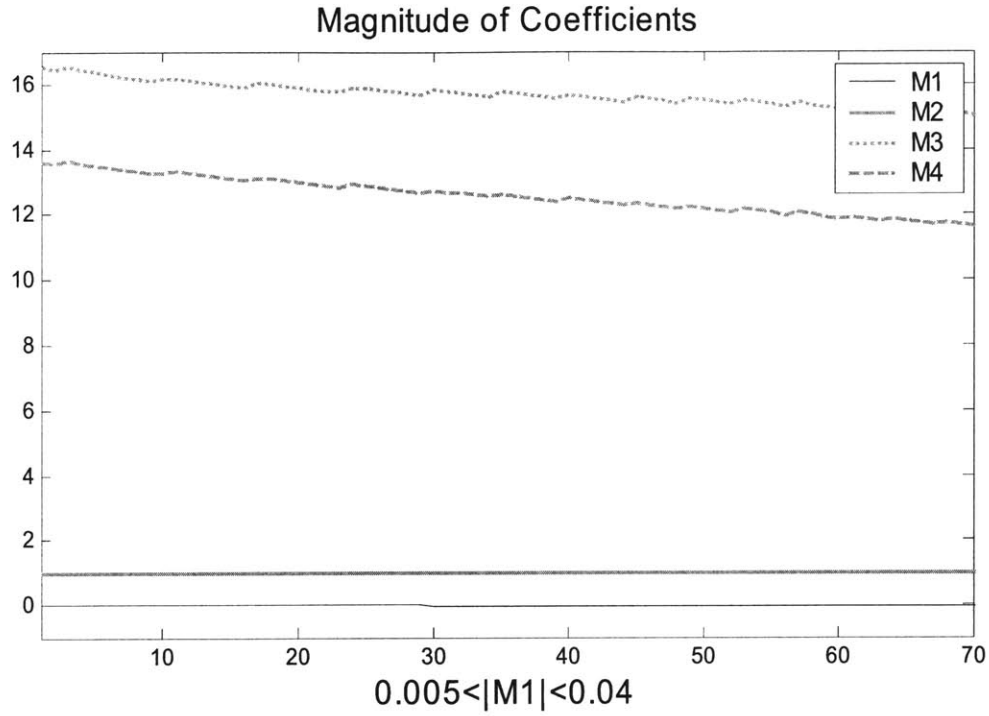

Figure 2.5 Magnitude of Coefficients for representative wheel-terrain interaction conditions

Equation 2.11 is a simplified version of Equation 2.9, and can be written as:

$$c = -M_3 * \tan\varphi + M_4 \tag{2.12}$$

Accuracy of this simplification plays an important role in successful estimation. This equation is linear, and its solution can be visualized as a straight line which has M_4 as its offset value on the y-axis and $-M_3$ as the slope.

If the simplified Equation 2.12 (which is the same with Equation 2.11) accurately represents the actual wheel-terrain interaction, then the line $y = -M_3 * x + M_4$ should near the point $(c,\ \tan\varphi)$ (see Figure 2.6). The deviance between this line and the point $(c,\ \tan\varphi)$ will be the error associated with Equation 2.11. Simulations on four representative terrain types with various terrain parameters and wheel operating conditions were performed to study this error. Table 2.1 shows the range of terrain characteristics used in simulations. The mean and standard deviation of these errors are $(\mu_c = 0.002,\ \sigma_c = 0.002)$ and $(\mu_{\tan\varphi} = 0.033,\ \sigma_{\tan\varphi} = 0.021)$.

Considering that the ranges of these parameters are $(0 \le c \le 10)$ and $(0.3 \le \tan\varphi \le 0.8)$, these results indicate that the simplified equation is sufficiently accurate (i.e. the errors are less than 10% of their actual value).

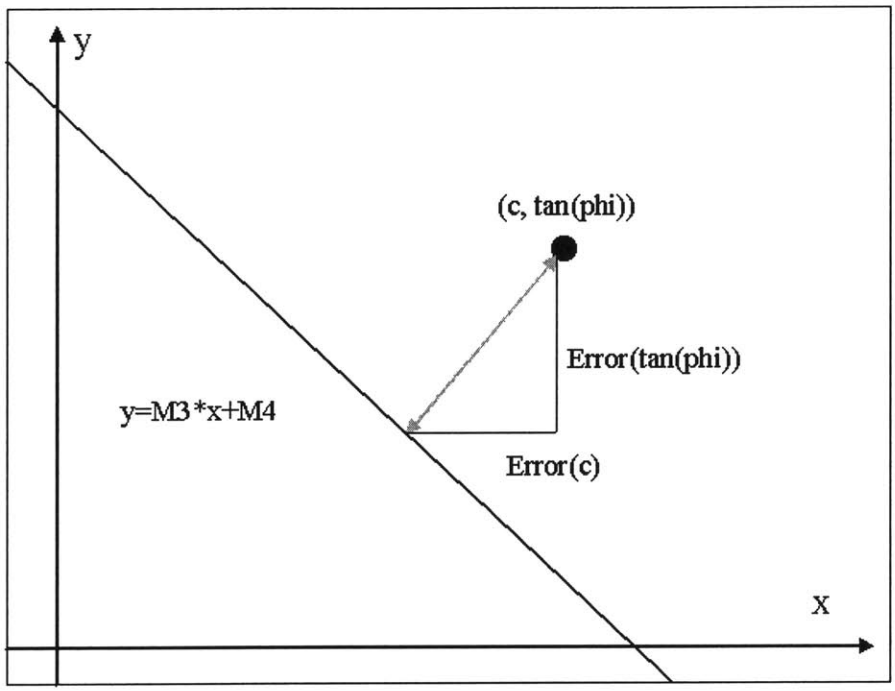

Figure 2.6 Simplification errors

The distance between line and point (M_3, M_4) is the approximation error.

Table 2.1 Terrain parameter range used in simulation

Terrain type	c (kPa)	ϕ (degree)	$\left[\frac{K_c}{b} + K_\phi\right]\left(kN/m^{n+2}\right)$
Sand	0 - 1	30 – 35	1500 – 2000
Clay	5 - 7	20 – 25	1000 – 1500
Loam	2 - 4	20 – 30	1500 – 2000
Firm soil	0 - 1	30 – 35	2500 - 3000

Parameter	n	K (m)	c_1	c_2
Range	0.5 – 1.2	0.01 – 0.03	0.43	0.32

As Equation 2.11 has two unknown parameters, c and φ can be determined with 2 equations. One set of experimental data on the wheel weight, torque, sinkage and slip ratio can determine one set of coefficients $(M_3,\ M_4)$ of Equation 2.10. Thus, the number of experimental data set is the number of equations in the form of Equation 2.11. When more than two equations (i.e. sets of data) are provided, c and φ can be determined by the least-square estimation method:

$$\begin{bmatrix} 1 & M_{31} \\ 1 & M_{32} \\ \vdots & \vdots \\ 1 & M_{3N} \end{bmatrix} \begin{bmatrix} c \\ \tan\phi \end{bmatrix} = \begin{bmatrix} M_{41} \\ M_{42} \\ \vdots \\ M_{4N} \end{bmatrix}, \qquad M_{iX} : M_i \ \ of \ \ Xth \ \ dataset \tag{2.13}$$

$$K_1 \begin{bmatrix} c \\ \tan\phi \end{bmatrix} = K_2 \quad where \quad K_1 = \begin{bmatrix} 1 & M_{31} \\ 1 & M_{32} \\ \vdots & \vdots \\ 1 & M_{3N} \end{bmatrix}, \quad K_2 = \begin{bmatrix} M_{41} \\ M_{42} \\ \vdots \\ M_{4N} \end{bmatrix} \tag{2.14}$$

$$K_1{}^T K_1 \begin{bmatrix} c \\ \tan\phi \end{bmatrix} = K_1{}^T K_2 \tag{2.15}$$

$$\begin{bmatrix} c \\ \tan\phi \end{bmatrix} = \left(K_1{}^T K_1\right)^{-1} \left(K_1{}^T K_2\right) \tag{2.16}$$

While computing the inverse $\left(K_1{}^T K_1\right)^{-1}$ in Equation 2.16, matrix conditioning is important. If the experimental data are almost the same, the matrix $\left(K_1{}^T K_1\right)$ becomes singular and the resulting estimation values will be inaccurate. To achieve a well-conditioned matrix, a large amount of data variation is recommended. Since the slip of a single wheel can often be controlled, it is desirable to introduce a large amount of slip ratio changes. In addition to the slip ratio changes, the wheel weight can vary if the terrain is uneven.

Figure 2.7 shows an example of estimation result on high-cohesion soil. Each black dot on the plot represents the data point (M_3, M_4) used in estimation. The slope of line fitted to the dots (gray line) is the estimated value of $\tan\varphi$ and the offset on the y-axis is the estimated cohesion. Black line represents the actual c (offset on y-axis) and $\tan\varphi$ (slope).

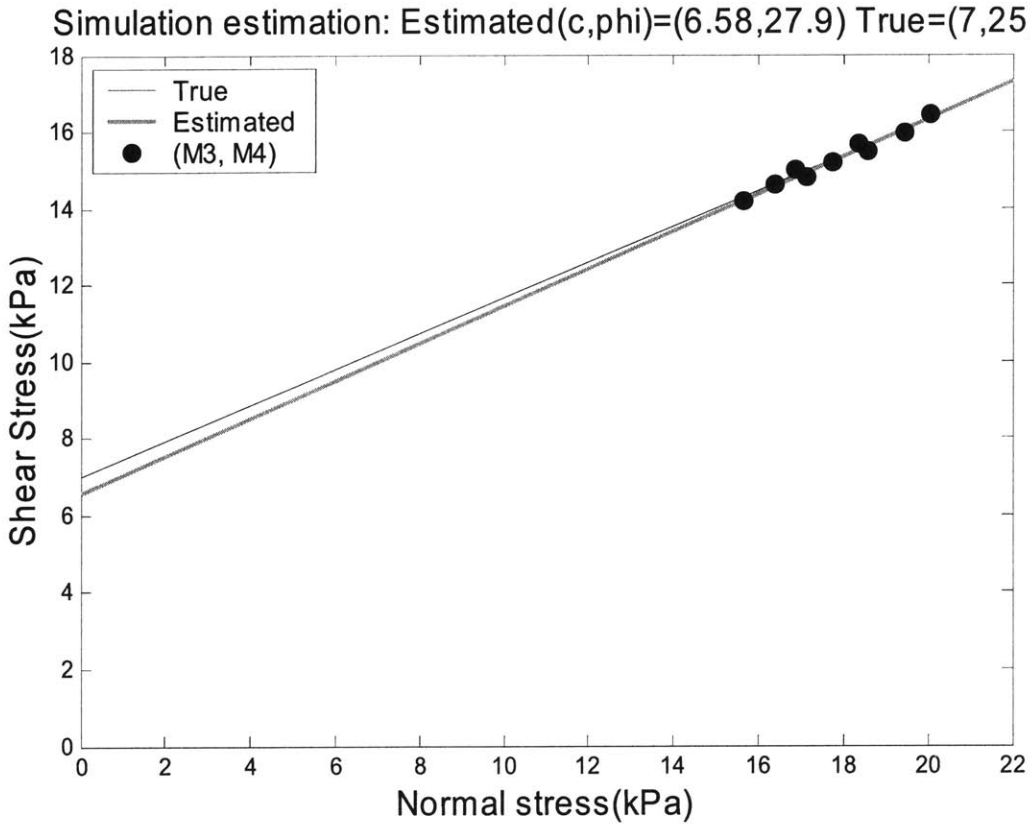

Figure 2.7 A representative simulation estimation result for cohesive terrain.
Estimation result shows close match to the true values on highly cohesive terrain (c=7 kPa).

Here a method for parameter estimation has been developed which is theoretically more accurate than previously proposed technics.

2.3 Simulation Results

Simulations of a single driven wheel traveling through deformable terrain were conducted in Matlab. The purpose of the simulation was to examine the accuracy of the parameter estimation algorithm in the presence of noisy and uncertain inputs. A single driven wheel traveling through deformable terrain was simulated. The wheel radius and width were 0.1 m each, and the wheel weight ranged from 60 to 100 N. These physical parameters were chosen to resemble JPL testbed rovers and actual Mars rover systems. Wong's rigid wheel – deformable terrain interaction model was used to compute the normal and shear stresses on the wheel-terrain interface [7]. Quasi-steady state analysis was assumed to calculate reaction stresses. This is valid due to the low speed of the system (less than 10 cm/s) [17].

At each step of simulation, all the reaction stresses were computed and integrated to obtain forces acting on the wheel. To accommodate disturbance and terrain uncertainty, small variations were added to resulting forces. Wheel motion due to these resulting forces were computed in each time step and new positions and velocities were calculated. This new state was used in next stress calculation. The wheel motor torque was controlled to set the wheel angular velocity and slip ratio, since the forward moving velocity of the system was fixed with small variation. At each step, wheel weight W, torque T, sinkage z, slip ratio *i*, forward velocity V and rotational velocity ω were recorded. Figure 2.8 shows a flowchart of this simulation.

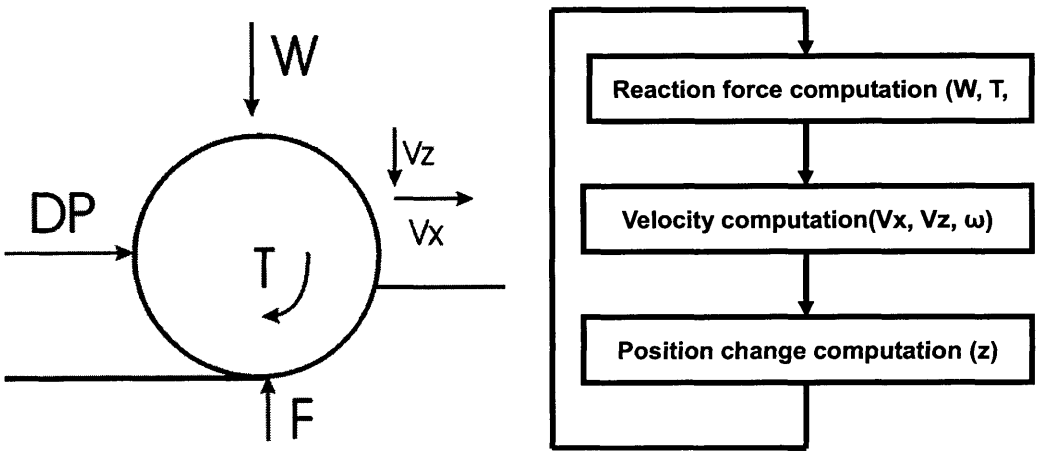

Figure 2.8 A schematic drawing of simulation steps

Terrain parameters c and φ can be estimated by Equation 2.16. The wheel slip ratio varied from 0.2 to 0.8, and the wheel linear velocity was set to be 2 cm/sec. With these settings, the maximum wheel rotational velocity was 10 cm/sec, and thus the system was slow enough to apply static analysis. Small variation was added to the wheel weight to simulate the effect of uneven terrain. The estimation process was as follow:

1. Wheel rotates at low slip ratio
2. Change slip ratio and wait until steady state is achieved
3. Measure and record wheel weight, torque, sinkage and slip ratio
4. Repeat step 2 and 3 until several data points are gathered
5. Put data into matrix form and compute estimated value of c and $\tan\varphi$

Simulations on 4 representative terrain types were conducted to examine the accuracy of the parameter estimation algorithm (see Table 2.1). Slip ratio increased by 0.1 every 1 second from 0.2 to 0.8. Once the slip ratio reached 0.8, it decreased by 0.1 until the slip ratio became 0.2. After that, the process repeated. Data sampling rate was set to 1 Hz to match the slip ratio change.

The number of data point used in the parameter estimation plays important role in accuracy and convergence of estimation values. Since the proposed method uses simplified equations and noisy sensor readings, the estimation values will show deviation from the actual values. As the number of data points used in estimation increases, the weight of the error on estimated values decreases. By using a large number of data, this deviation can be minimized.

Figure 2.9 shows the effect of increasing number of data points used in the estimation process. As the number of data points used in the estimation process increases, the accuracy and the convergence of the estimated values also increases. If the quality of data (i.e. signal to noise ratio) is consistent, increasing the number of data significantly enhances the estimation results.

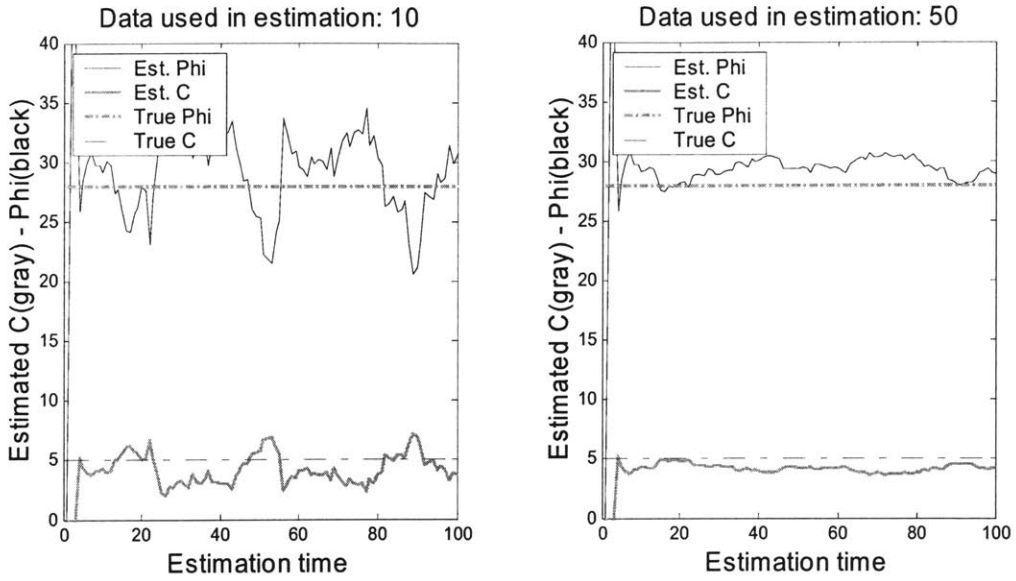

Figure 2.9 Effect of increasing number of data points used in estimation

As the number of data points used in estimation becomes larger, the estimation result shows better convergence.

Simulation results on these estimation conditions show that RMS errors in c and φ estimations are 1.14kPa and 6.52° respectively when 5% white noises are added to all measurements. In general, less than 5% signal to noise ratio is expected and thus 5% noises are used in estimation. 10 data points were used in the estimation. Considering that the range of true c and φ are $(0 \le c \le 7)$ and $(20 \le \varphi \le 35)$, it can be concluded that the proposed estimation method works well with noisy measurements.

2.4 Experimental Validation

Experimental validation of proposed estimation method was conducted on the Field and Space Robotics Laboratory terrain characterization testbed (see Figure 2.10). The testbed was used to experimentally estimate the characteristics of three different types of soils. Estimated c and φ were compared with reference values, which were obtained from traditional characterization method (Bevameter experiment).

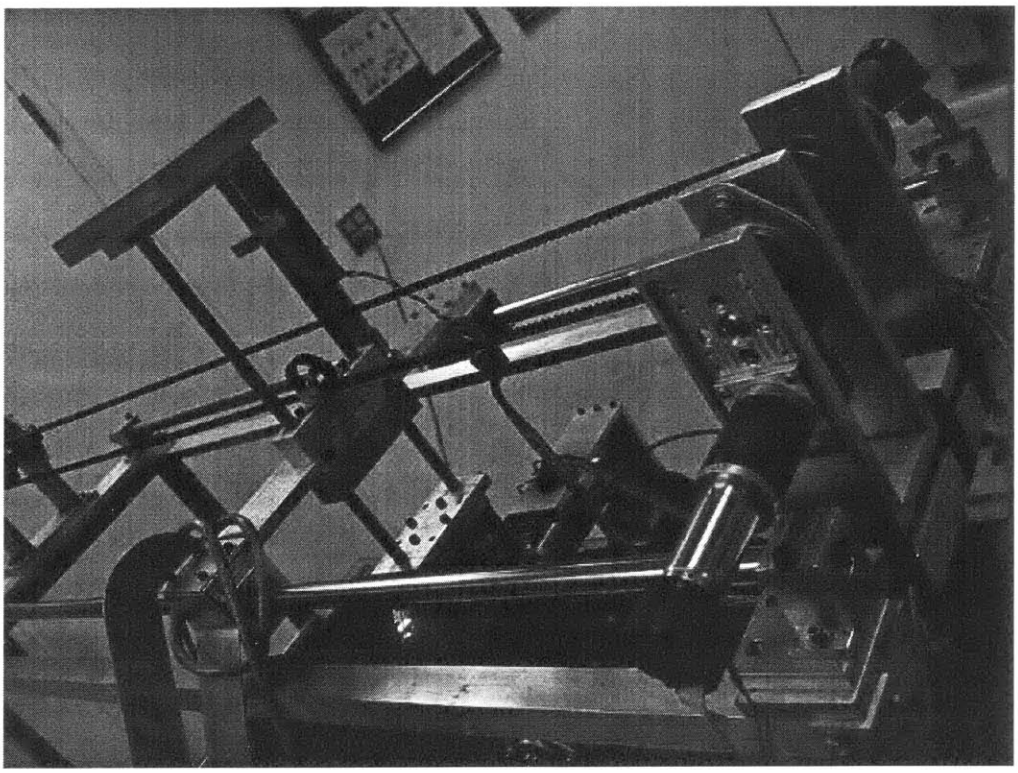

Figure 2.10 FSRL wheel-terrain interaction testbed

The testbed consists of a driven rigid wheel mounted on an undriven vertical axis. The wheel dimensions are 0.1 m radius and 0.05 m width with 0.54 kg mass. The wheel assembly can move freely in the vertical direction. The wheel-axis assembly is mounted to a driven horizontal carriage. The wheel motor is controlled by a voltage control unit which can supply 15V 3A at maximum capacity. A tachometer attached to the wheel motor is used to measure

wheel rotational velocity. The carriage motor is controlled by a PWM circuit with maximum capacity of 25V 3A. A 2048 PPR encoder is used to measure the rotational velocity of the carriage pulley and the carriage linear velocity is computed from the carriage pulley angular velocity. By driving the wheel and carriage at different rates, variable slip ratios can be imposed. The maximum wheel angular velocity is 1.5 rad/sec. This results in a maximum linear velocity of 15.0 cm/sec. The maximum carriage pulley angular velocity is 2 rad/sec, which results in a maximum carriage linear velocity of 5 cm/sec. In normal operation mode, the slip ratio ranges from 0 to 0.93.

The vertical load on the wheel can be arbitrarily chosen by adding weights to the vertical axis. Five different weights were applied to the testbed ranging from 5.42kg to 8.51kg. A rotating torque sensor is positioned between the wheel and wheel motor and used to measure wheel torque. The torque sensor has a working range of ± 7Nm and the output voltage is 3.0mV/Nm. A x200 operational voltage amplifier is used to magnify the torque sensor output signal. The vertical wheel sinkage is measured with a linear potentiometer. Due to the placement of the motor and the rotational torque sensor, wheel sinkage is limited to 0.065 m. This is 65% of the wheel radius. The six-component wrench between the wheel and carriage is measured with an AMTI six-axis force/torque sensor. The force/torque sensor allows measurement of the normal load W and drawbar pull DP. The force-torque sensor has maximum capacity of 900N and $\pm 0.1\%$ error on maximum capacity, which is about 0.9N.

All sensor measurements and control signals are recorded or generated by an 8-axis 12 bit I/O board of working range ± 10V. The resolution of the I/O board is 5mV. The control and measurement algorithm is run on an Intel 486 66 Mhz processor at a rate of 100 Hz. A soilbin of 0.9 m long, 0.3 m wide and 0.15 m deep is used to contain the experimental material (soil). The depth of soil bin is chosen to exceed 1.5 times the maximum allowable sinkage.

Terrain characteristics of three different soil types (dry sand, dry bentonite clay and compacted topsoil) were first measured by Bevameter experiments (see Appendix B). Green lines in each Bevameter estimation plots represent the estimation results $y = \tan\phi \cdot x + c$. These "traditional" measurements were taken as the reference values for c and φ. Figure 2.11~2.13, Table 2.2 and Table 2.3 show the measured reference values and published data for similar terrain types [18,19,20].

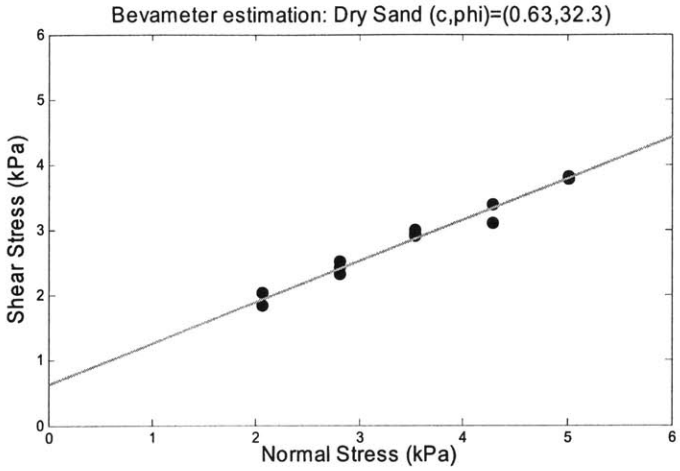

Figure 2.11 Bevameter experiment on dry sand

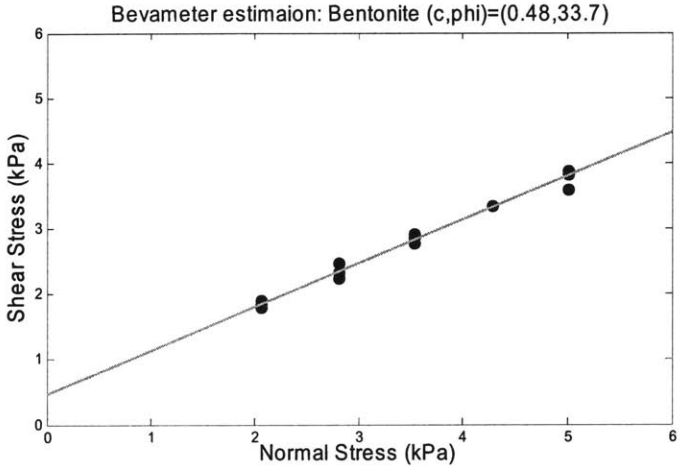

Figure 2.12 Bevameter experiment on bentonite clay

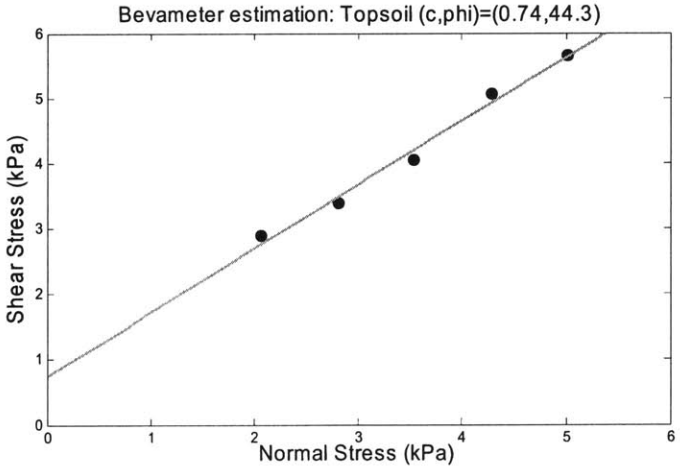

Figure 2.13 Bevameter experiment on compacted topsoil

Table 2.2 Soil characterization results

Soil Type	Estimation method	Cohesion (kPa)	Internal friction angle (degree)
Dry sand	Bevameter	0.63	32.3
Dry bentonite clay	Bevameter	0.46	33.7
Compacted topsoil	Bevameter	0.74	44.3

Table 2.3 Published terrain cohesion and internal friction angle

Terrain type	Cohesion (kPa)	Internal friction angle (degree)
Sand	0.36 – 1.39	24 – 36
Clay	1.85 – 68.95	6 – 34
Sandy loam	1.1 – 13.79	11 – 39.4
Clayey soil	1.85 – 7.58	9.7 – 14
Medium soil	8.62	22.5
Soft soil	3.71	25.6
Martian soil	0 – 5.1	18 – 42.4
Muskeg	0.5 - 59	27.9 – 51.6
Martian soil	0 – 5.1	18 – 42.4

The estimation process was: 1) set a target slip ratio 2) after achieving steady state, record sensory data 3) move on to next target slip ratio. Due to the limited length of testbed operation space, only one steady state slip ratio could be achieved per testbed length. Thus multiple runs were used in a single experiment. Once all the slip ratios were achieved, the data were collected and analyzed altogether. Shear deformation modulus K of each terrain was

determined before the analysis was performed (see Appendix D). Figure 2.14 ~2.16 and Table 2.4 show the estimation results on dry sand, dry bentonite clay and wet topsoil. The number of data points used in the estimation was 20.

It can be seen that after an initial transient stage, the estimation values converge to steady values. The estimation difference from the reference values may come from various reasons:

1) Estimation error: estimation algorithm itself contains inaccurate formulation and can cause error on results

2) Noisy signal: sensor readings incorporate errors which play a significant role in estimation

3) Inaccurate measurement: measurement can have offset from the true values due to inaccurate sensor calibration

4) Terrain homogeneity: terrain can contain other substances such as small rocks and other soils. Inhomogeneous terrain can lead to inaccurate estimation results.

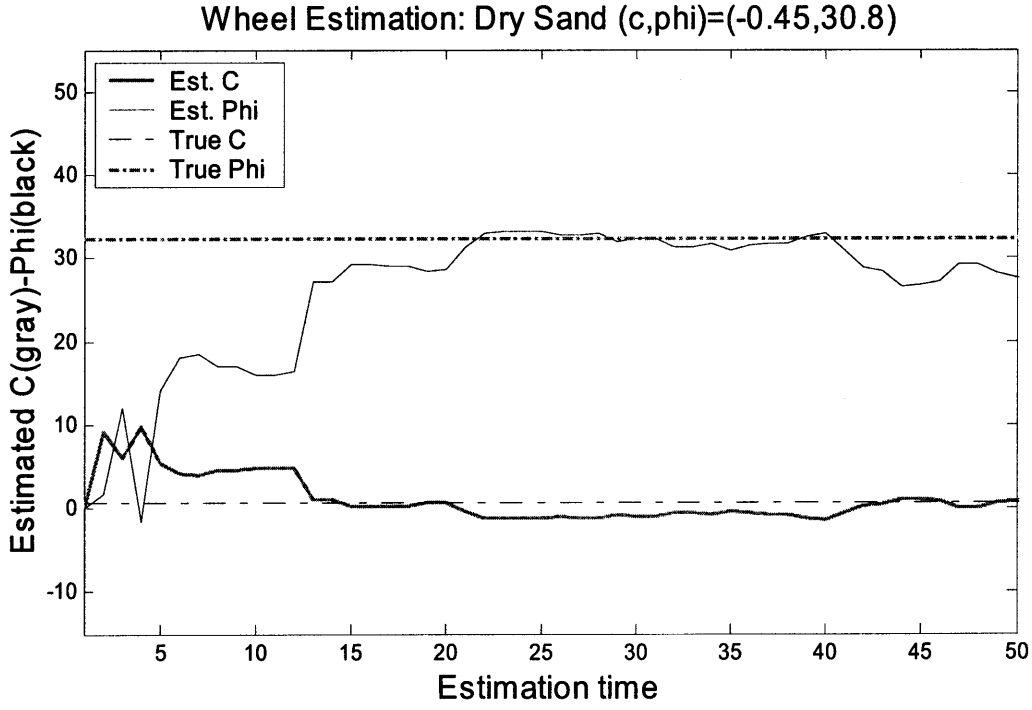

Figure 2.14 Estimation result on dry sand

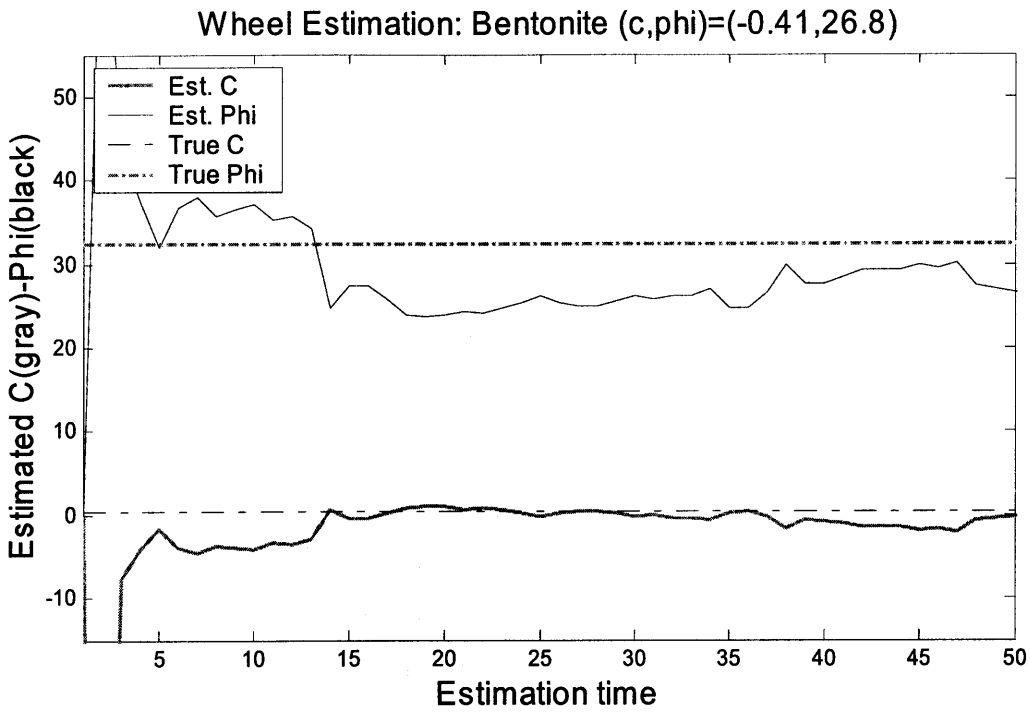

Figure 2.15 Estimation result on dry bentonite clay

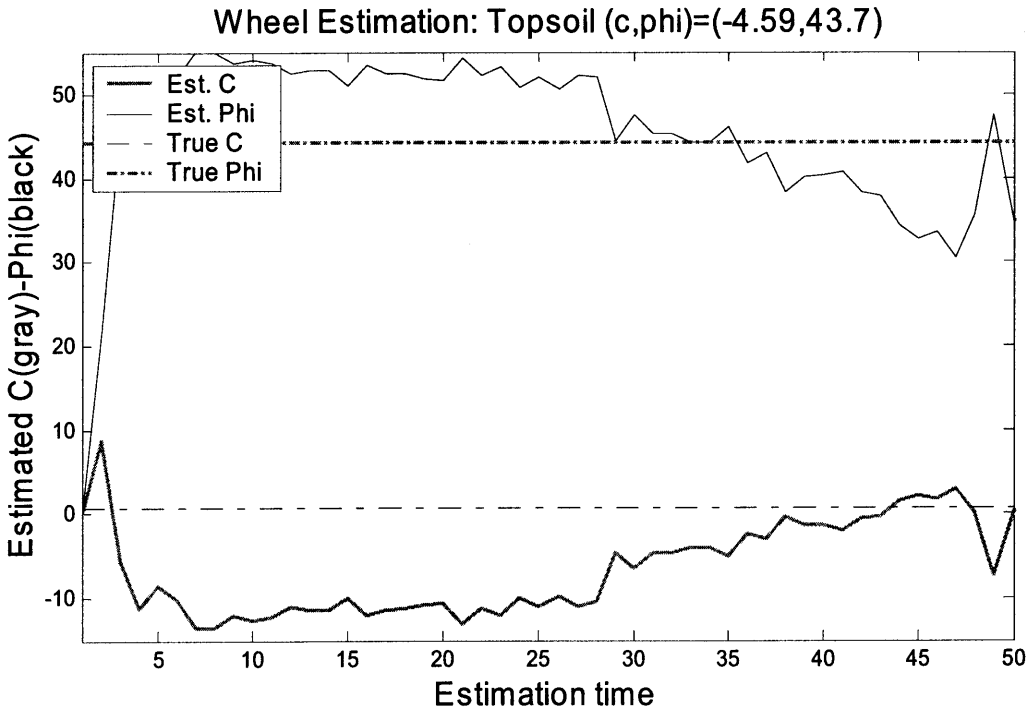

Figure 2.16 Estimation result on compacted topsoil

Considering the range of c and tanφ, terrain characteristics estimation results by the proposed method show good agreement with both published data and results of the Bevameter terrain characterization. Errors from noise and estimation algorithm can be minimized by using multiple data points in estimation. Improved sensor calibration can reduce the accuracy of sensor measurement.

This concludes that the proposed estimation method can accurately measure the terrain characteristics of many different terrain types. Since the method uses small resources and computation time, it can be used on a terrestrial exploration rover to perform on-line estimation.

Chapter 3: Traversability Prediction

3.1 Introduction

In planetary exploration mission, rovers are required to traverse challenging environments to interesting scientific areas (see Figure 3.1). Since a rover cannot be controlled by human operators in real time, it must be capable of planning and following a safe path autonomously. Path-planning on rough terrain should take into account many aspects related to rover safety, such as physical configuration, limits, the existence of geometric obstacles and terrain characteristics. Many researchers have studied path-planning methods that consider geometric obstacles, slope and roughness of terrain. To successfully plan a safe path, however, terrain characteristics such as terrain traversability should also be considered. Traversability can be defined as the amount of forward thrust a wheel can generates in a given terrain region. Few researchers have studied traversability estimation. In this chapter, a method which can assess traversability of deformable terrain using on-board rover sensors is presented.

Among many parameters describing terrain characteristics, the most meaningful one in terms of mobility is the drawbar-pull (DP), or the thrust force a vehicle exerts on the terrain. A large positive drawbar-pull means that the terrain is easy to traverse. On the other hand, if the drawbar-pull is small or negative, the vehicle cannot easily traverse the terrain and may get trapped. Thus, terrain traversability can be described with drawbar-pull. A positive and large

drawbar-pull has 'good' traversability, and small or negative drawbar-pull has 'bad' traversability.

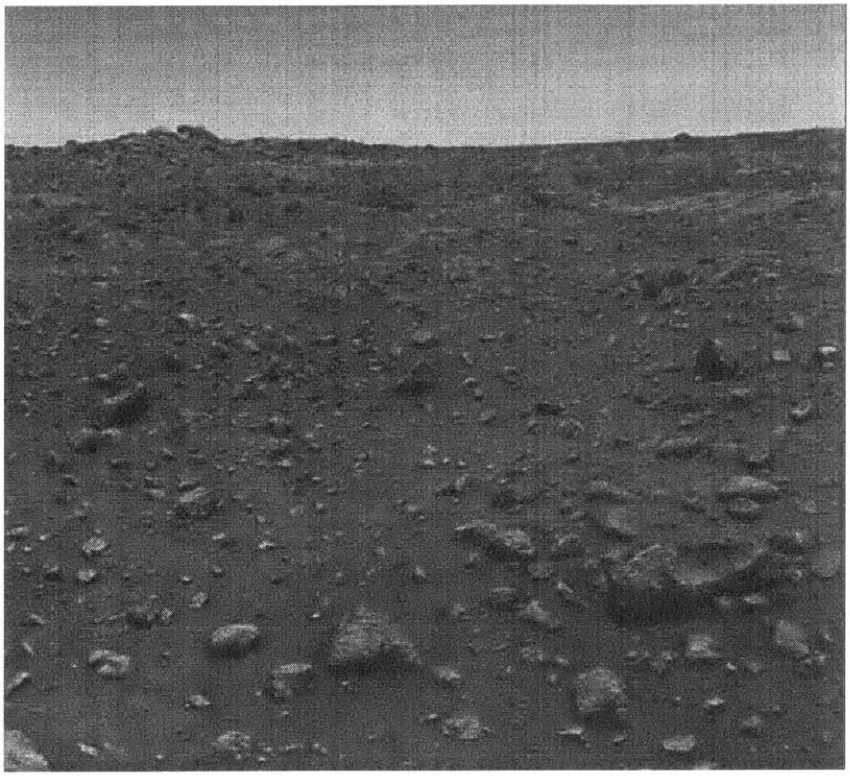

Figure 3.1 Viking landing site (Mars Pathfinder website: http://mars.jpl.nasa.gov/MPF)

In a laboratory setting, we can use a force sensor to measure DP with respect to a reference frame which doesn't accelerate. In real rover settings, this reference frame doesn't exist and the use of a force sensor to measure DP is impossible. A method to estimate DP using simple sensor data and minimal computation will be presented and experimentally validated. A method for predicting the traversability from DP will also be discussed.

3.2 Theoretical Analysis

In Chapter 2, a method for approximation of stress distribution on the wheel-terrain interface

was discussed along with the computation of reaction forces W and T. In similar way, drawbar-pull DP can be also calculated from the simplified stress distributions. The nonlinear form of the DP computation is [18]:

$$DP = rb\int_0^{\theta_1}(\tau\cos\theta - \sigma\sin\theta)d\theta \tag{3.1}$$

From Equation 3.1, DP could be computed by assuming a linear-offset stress distribution at the wheel-terrain interface and using estimated c and φ values to compute σ and τ (see Chapter 2). This method requires only measurements of the wheel weight, torque, sinkage and slip ratio, and these parameters can be easily measured with on-board rover sensors or estimated from other parameters. However, the estimation of c and φ takes time and contains uncertainty. Also, to perform terrain parameter estimation, the rover must traverse unknown terrain until it gathers sufficient amount of sensor data. In some cases, it is undesirable for a rover to traverse potentially dangerous terrain without any information about its characteristics. Since a goal is to avoid dangerous terrain, an alternative method that estimates DP without risking rover safety would be appropriate.

In estimating DP, three factors play important roles: terrain characteristics, wheel physical properties and wheel operating condition. Once all these factors are known, the resulting forces and sinkage are uniquely determined by the wheel-terrain interaction equations (see Appendix C). The equations for T, z and DP are functions of the parameters related to the terrain, wheel and operating conditions. Among these parameters, wheel physical properties, operating conditions (i.e. the slip ratio *i*), wheel torque T and sinkage z are easily obtainable from sensors or prior experiments. If the terrain characteristics can be estimated from the reaction torque T, sinkage z, wheel physical properties, and the operating condition, it can also be used to estimate DP. Furthermore, if the intermediate state of estimating terrain characteristics can be omitted, DP can be directly estimated from T, z, wheel physical properties, and operating condition. The information flow can be seen in Figure 3.2.

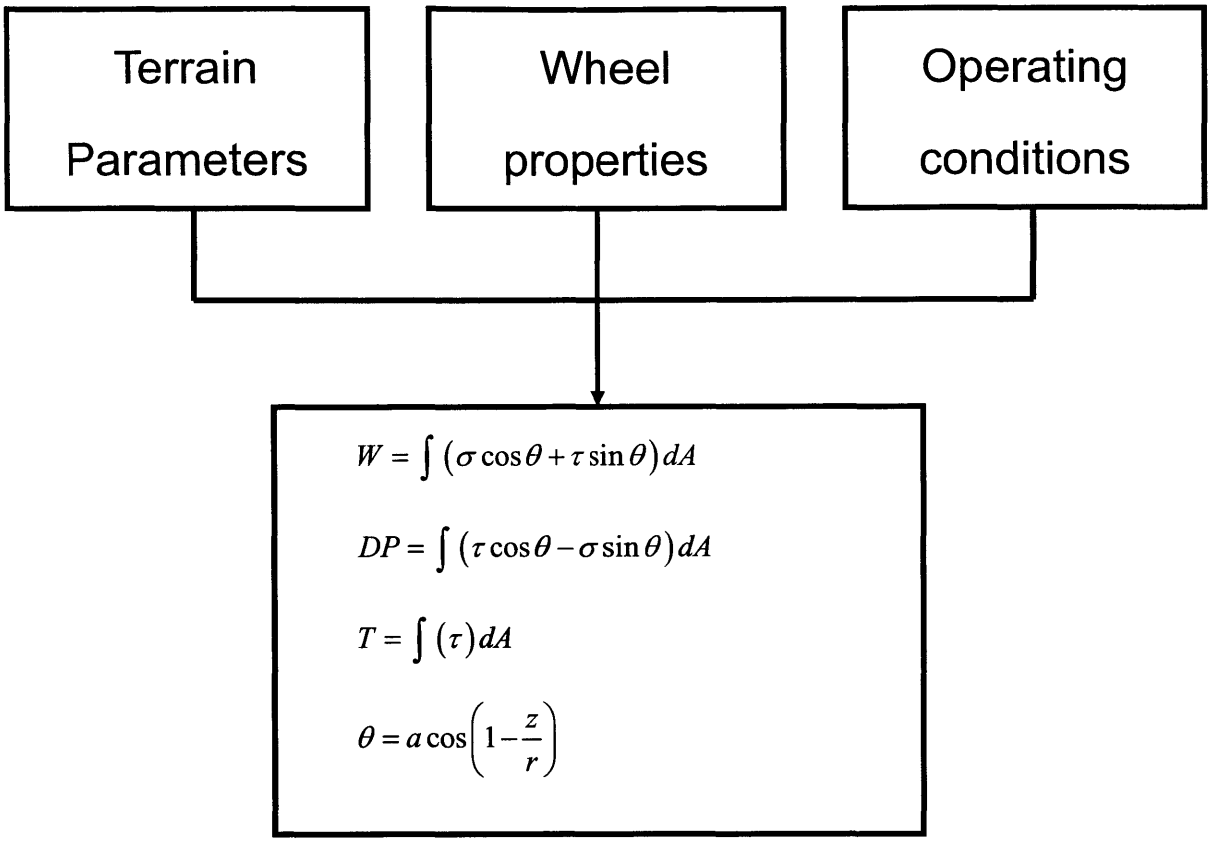

Figure 3.2 Information flow of wheel-terrain interaction.
Information on terrain parameters, wheel physical properties and operating conditions are combined to produce reaction forces.

To accomplish this, we first simplify the force equilibrium equations. The sum of all forces acting at the wheel-terrain interface can be represented as a pair of forces X and Y (see Figure 3.3). The angle of force action θ is a function of W, T and DP. With knowledge on the weight W, wheel torque T, and the angle of force action θ, X and Y can be computed as follows:

$$W = X\sin\theta + Y\cos\theta, \quad T = rX \tag{3.2}$$

$$X = \frac{T}{r}, \quad Y = \frac{(W - A\sin\theta)}{\cos\theta} = \frac{1}{\cos\theta}W - \tan\theta\frac{T}{r} \tag{3.3}$$

The resulting drawbar-pull DP can be estimated as follows:

$$DP = X\cos\theta - Y\sin\theta = \cos\theta\frac{T}{r} - \sin\theta\left(\frac{1}{\cos\theta}W - \tan\theta\frac{T}{r}\right)$$
$$= \left(\cos\theta + \sin\theta\tan\theta\right)\frac{T}{r} - \tan\theta W = \frac{1}{\cos\theta}\frac{T}{r} - \tan\theta W \qquad (3.4)$$
$$\cong \frac{T}{r} - \theta W \quad (with\ \ small\ \ angle\ \ approximation)$$

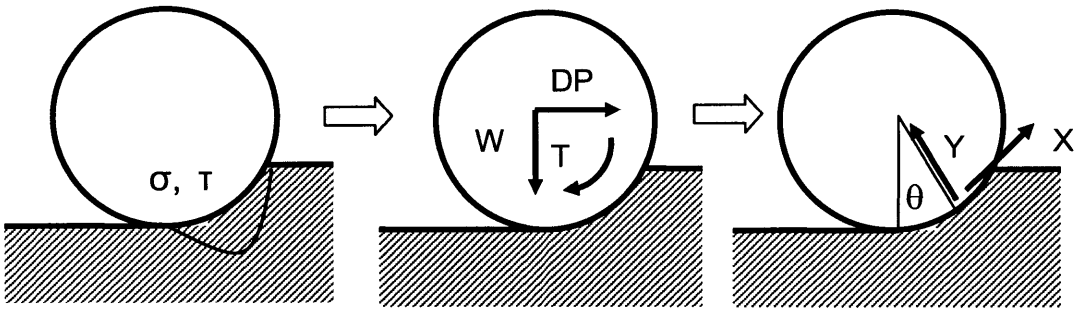

Figure 3.3 Force reconstruction.

The stresses can be summed up to find out the reaction forces W, T and DP. These three forces can be reconstructed with two forces X and Y acting at around the center of wheel-terrain interface

Equation 3.4 shows that a simplified relationship can be written to describe the relationship between DP, W, T and θ. Since Equation 3.4 is a simplification of the nonlinear equations, error is expected. A dimensionless form of this equation can be written with three dimensionless variables $\frac{DP}{W}$, $\frac{T}{rW}$ and θ:

$$\frac{DP}{W} \cong \frac{T}{rW} - \theta \qquad (3.5)$$

Considering the geometry of wheel-terrain contacting patch and shape of stress profiles, we

can assume that θ will be around $\theta = \frac{\theta_1}{2}$ without loss of generality (see Appendix B).

$$\frac{DP}{W} \cong \frac{T}{rW} - \frac{\theta_1}{2} \tag{3.6}$$

An alternative simplification of the stress distribution equations leads to similar results. Iagnemma suggested a linear approximation of normal and shear stress distribution at the wheel-terrain interface [17]. This method tends to ignore the effect of cohesion c, but can be applied with reasonable accuracy to terrains with low or moderate cohesion. With the linear stress approximation, the stress distribution can be written as follows:

$$\sigma_1(\theta) = \frac{2(\theta_1 - \theta)}{\theta_1}\sigma_m \quad \left(\frac{\theta_1}{2} \le \theta \le \theta_1\right), \qquad \sigma_2(\theta) = \frac{2\theta}{\theta_1}\sigma_m \quad \left(0 \le \theta \le \frac{\theta_1}{2}\right)$$

$$\tau_1(\theta) = \frac{2(\theta_1 - \theta)}{\theta_1}\tau_m \quad (\theta_m \le \theta \le \theta_1), \qquad \tau_2(\theta) = \frac{2\theta}{\theta_1}\tau_m \quad (0 \le \theta \le \theta_m) \tag{3.7}$$

Drawbar-pull (DP) can be computed by integrating these stresses over the wheel-terrain contact area:

$$DP = \int_0^{\theta_1} \left(\tau_2(\theta)\cos\theta - \sigma_2(\theta)\sin\theta\right) dA + \int_{\theta_m}^{\theta_1} \left(\tau_1(\theta)\cos\theta - \sigma_1(\theta)\sin\theta\right) dA$$

$$= rb\int_0^{\theta_1} \left(\tau_2(\theta)\cos\theta - \sigma_2(\theta)\sin\theta\right) d\theta + rb\int_{\theta_m}^{\theta_1} \left(\tau_1(\theta)\cos\theta - \sigma_1(\theta)\sin\theta\right) d\theta \tag{3.7}$$

$$= \frac{2rb}{\theta_1}\left(\left(2\cos\frac{\theta_1}{2} - \cos\theta_1 - 1\right)\tau_{max} - \left(2\sin\frac{\theta_1}{2} - \sin\theta_1\right)\sigma_{max}\right)$$

σ_{max} and τ_{max} can be derived from the force balance equations on W and T:

$$T = \int_0^{\theta_1} \tau(\theta)\, dA = \frac{r^2 b \theta_1 \tau_{max}}{2} \tag{3.8}$$

$$\tau_{max} = \frac{2T}{r^2 b \theta_1} \tag{3.9}$$

$$\begin{aligned} W &= \int_0^{\theta_1} \left(\sigma(\theta)\cos\theta + \tau(\theta)\sin\theta\right) dA \\ &= \frac{2rb}{\theta_1}\left(\left(2\cos\frac{\theta_1}{2} - \cos\theta_1 - 1\right)\sigma_{max} + \left(2\sin\frac{\theta_1}{2} - \sin\theta_1\right)\tau_{max}\right) \end{aligned} \tag{3.10}$$

$$\begin{aligned} \sigma_{max} &= \frac{\frac{\theta_1}{2rb}W - \left(2\sin\frac{\theta_1}{2} - \sin\theta_1\right)\tau_{max}}{2\cos\frac{\theta_1}{2} - \cos\theta_1 - 1} \\ &= \frac{\frac{\theta_1}{2rb}W - \left(2\sin\frac{\theta_1}{2} - \sin\theta_1\right)\frac{2}{r^2 b\theta_1}T}{2\cos\frac{\theta_1}{2} - \cos\theta_1 - 1} \end{aligned} \tag{3.11}$$

DP can thus be described as a function of W, T and $\theta_1 = \tan^{-1}\left(1 - \frac{z}{r}\right)$:

$$\begin{aligned} DP &= \frac{2rb}{\theta_1}\begin{pmatrix} \left(2\cos\frac{\theta_1}{2} - \cos\theta_1 - 1\right)\frac{2T}{r^2 b\theta_1} \\ -\left(2\sin\frac{\theta_1}{2} - \sin\theta_1\right)\frac{\frac{\theta_1 W}{2rb} - \left(2\sin\frac{\theta_1}{2} - \sin\theta_1\right)\frac{2T}{r^2 b\theta_1}}{\left(2\cos\frac{\theta_1}{2} - \cos\theta_1 - 1\right)} \end{pmatrix} \\ &= -\frac{\left(2\sin\frac{\theta_1}{2} - \sin\theta_1\right)}{\left(2\cos\frac{\theta_1}{2} - \cos\theta_1 - 1\right)}W + \frac{\left(2\cos\frac{\theta_1}{2} - \cos\theta_1 - 1\right)^2 + \left(2\sin\frac{\theta_1}{2} - \sin\theta_1\right)^2}{\left(2\cos\frac{\theta_1}{2} - \cos\theta_1 - 1\right)}\frac{4}{\theta_1^2}\frac{T}{r} \end{aligned} \tag{3.12}$$

In real-world situations, $\theta_1 = \cos^{-1}\left(1-\frac{z}{r}\right)$ is generally smaller than 60° $\left(z \le \frac{r}{2}\right)$. This enables small angle approximations to be written for the second order polynomials. The DP can be rewritten as:

$$\left(2\sin\frac{\theta_1}{2}-\sin\theta_1\right)\cong\frac{\theta_1^3}{8},\qquad \left(2\cos\frac{\theta_1}{2}-\cos\theta_1-1\right)\cong\frac{\theta_1^2}{4} \tag{3.13}$$

$$DP=-\frac{\theta_1^3}{8}\frac{4}{\theta_1^2}W+\frac{\frac{\theta_1^4}{16}+\frac{\theta_1^6}{64}}{\frac{\theta_1^2}{4}}\frac{4}{\theta_1^2}\frac{T}{r}=-\frac{\theta_1}{2}W+\left(1+\frac{\theta_1^2}{4}\right)\frac{T}{r}\cong\frac{T}{r}-\frac{\theta_1}{2}W \tag{3.14}$$

$$\frac{DP}{W}\cong\frac{T}{rW}-\frac{\theta_1}{2} \tag{3.15}$$

Equations 3.5 and 3.15 show similar results for drawbar-pull estimation from wheel weight W, torque T, radius r and sinkage z. The similarity of these equations suggests that a simple relationship between DP and the parameters W, T and z exists.

3.3 Simulation Results

Wheel-terrain interaction simulations were conducted using Wong's model of wheel-terrain interaction to study the accuracy of the DP estimation equations derived in Section 3.2. Four representative terrain types were used in simulation to consider the effect of terrain variation on estimation accuracy. Within each terrain type, terrain parameters varied in a pre-defined range. Wheel operating conditions were also changed. The weight and slip ratio of the wheel were

varied stepwise to study the effect of wheel physical properties and operating condition. See Table 2.1 for terrain types and the terrain parameter ranges used in the simulation. The dimensions of the wheel were fixed as radius 0.1m and width 0.1m. These were chosen to resemble the FIDO experimental rover at JPL and the Mars Sojourner rover (see Figure 3.4) [10].

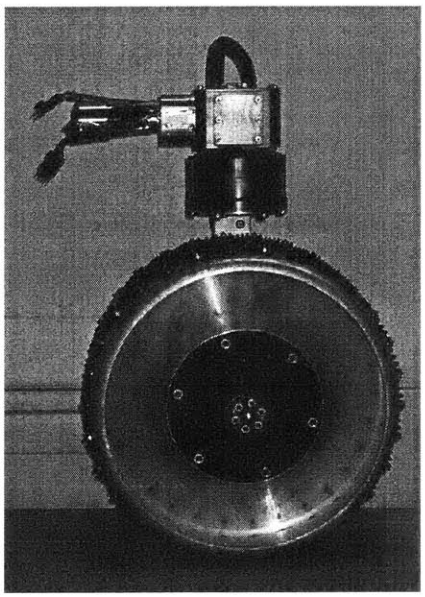

Figure 3.4 FIDO rover wheel. Wheel radius and width are 0.1 m and 0.125 m

To study the dependence of DP on the variables T, W and z, and terrain parameters c, φ, n, K, k_c and k_φ, DP was plotted against T and z for a fixed W. Nonlinear wheel-terrain interaction equations (Equation C.2~C.10, see Appendix C) were used to compute DP. Note that although W, T, and z are fixed, terrain parameters such as c and φ are allowed to vary. Figure 3.5 shows data from all four terrain types used in the simulations. The low variance of DP, given T, W, and z, suggests that if W, T and z are given, DP can be reasonably estimated over wide variety of terrain types and wheel operating conditions. Thus it is not necessary to measure or estimate c or φ to predict DP with reasonable accuracy.

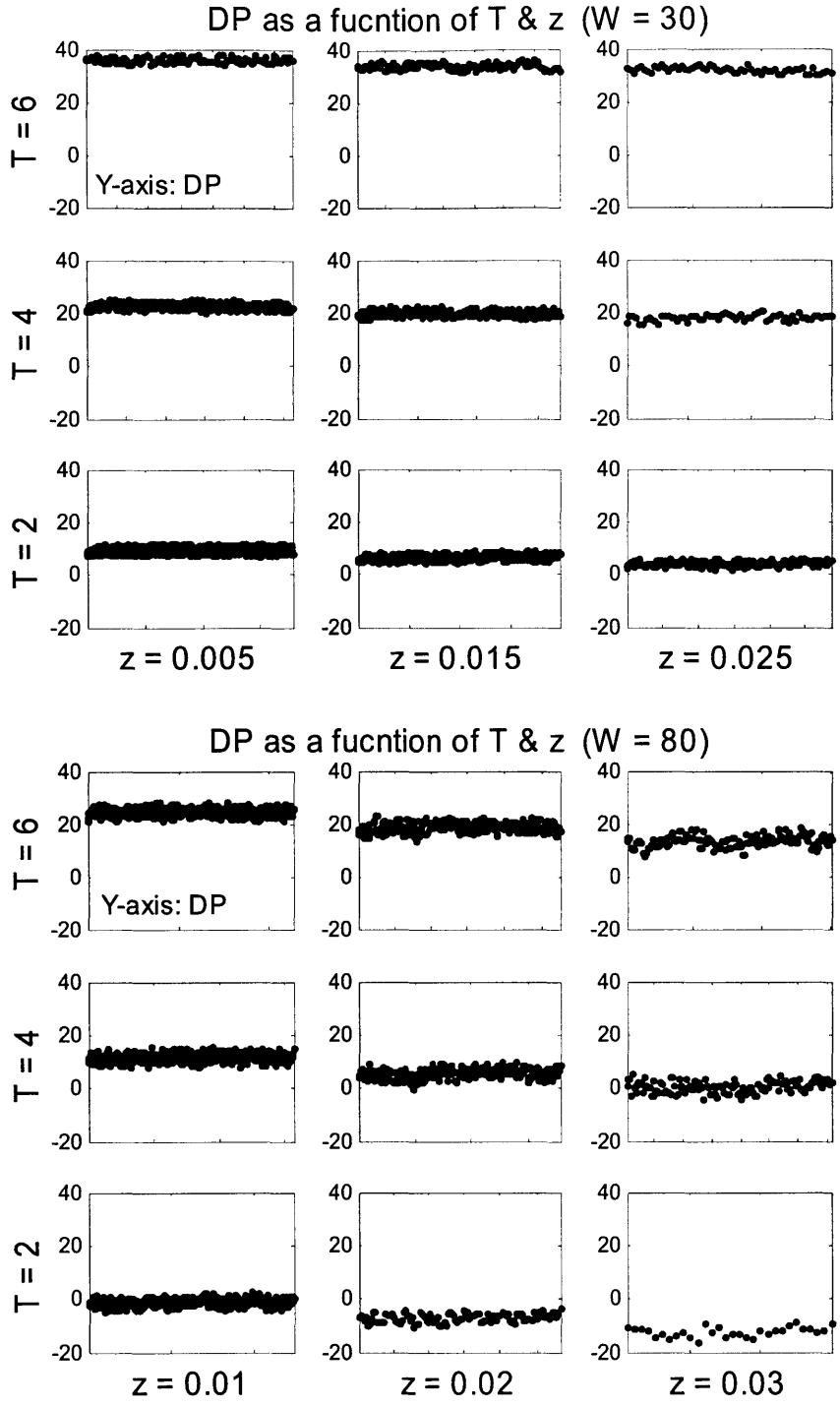

Figure 3.5 Dependence of DP on W, T and z.

y-axis on each subplots is DP, and x-axis is variety of terrain type with given z and T conditions. Even though terrain types and operating conditions are different, if W, T and z are similar, the resulting DP are almost the same.

A similar plot using dimensionless variables $\frac{DP}{W}$, $\frac{T}{rW}$ and $\frac{z}{r} \approx \theta_1$ shows a similar result (see Figure 3.6). By using dimensionless variables, the number of parameters can be reduced from four (W, T, z and DP) to three ($\frac{DP}{W}$, $\frac{T}{rW}$ and $\frac{z}{r}$). This result suggests that the dimensionless parameters can successfully describe a wide variety of terrains.

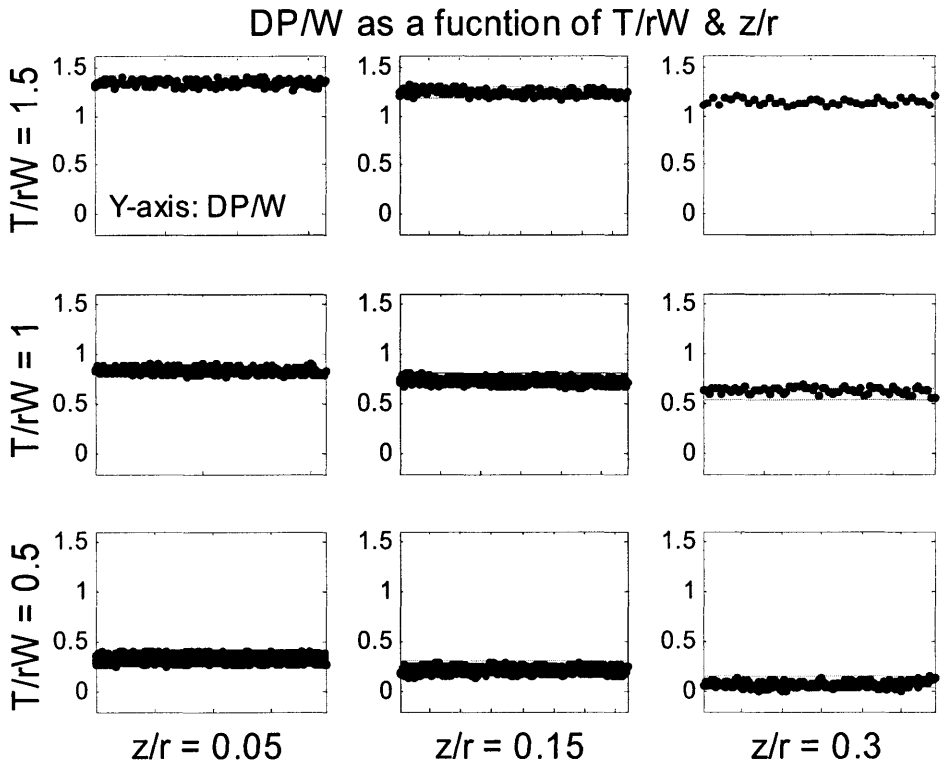

Figure 3.6 DP estimation using dimensionless variables.

Dimensionless parameters $\frac{DP}{W}$, $\frac{T}{rW}$ and $\frac{z}{r} \approx \theta_1$ are grouped and plotted according to $\frac{T}{rW}$ and $\frac{z}{r} \approx \theta_1$. The small variance of $\frac{DP}{W}$ implies that $\frac{DP}{W}$ is a function of $\frac{T}{rW}$ and $\frac{z}{r} \approx \theta_1$. Gray line is the range of DP in simulation data.

The two simplified relations suggest that $\frac{DP}{W}$ has a linearly positive dependence on $\frac{T}{rW}$ and negative dependence on $\frac{z}{r}$. Simulations were performed to study the accuracy of these equations in predicting DP. Terrains ranging from sandy and cohesionless soil to firm and cohesive soil were considered in simulation. A plane fit was performed to determine constant "correction factors" to these equations:

$$\frac{DP}{W} = C_1 \cdot \frac{T}{r \cdot W} + C_2 \cdot \frac{z}{r} + C_3 \tag{3.16}$$

$$A \cdot \begin{bmatrix} C_1 \\ C_2 \\ C_3 \end{bmatrix} = B \tag{3.17}$$

where A and B are data from a nonlinear simulation:

$$A = \begin{bmatrix} \left(\frac{T}{rW}\right)_1 & \left(\frac{z}{r}\right)_1 & 1 \\ \vdots & \vdots & \vdots \\ \left(\frac{T}{rW}\right)_N & \left(\frac{z}{r}\right)_N & 1 \end{bmatrix}, \quad B = \begin{bmatrix} \left(\frac{DP}{W}\right)_1 \\ \vdots \\ \left(\frac{DP}{W}\right)_N \end{bmatrix} \tag{3.18}$$

$$\begin{bmatrix} C_1 \\ C_2 \\ C_3 \end{bmatrix} = \left(A^T A\right)^{-1} A^T B \tag{3.19}$$

By putting the data from the simulation result, coefficients of the estimation equation can be determined:

$$[C_1 \quad C_2 \quad C_3] = [1 \quad -1 \quad -0.1] \tag{3.20}$$

Thus the "corrected" DP estimation equation can be written as:

$$\frac{DP}{W} = \frac{T}{rW} - \frac{z}{r} - 0.1 \tag{3.21}$$

Results comparing estimation of DP with Equation 3.21 to a nonlinear computation show a small deviance on all the terrain types and wheel operating condition. The mean and standard deviation of the estimation error from the computed DP values for all four terrain types and operating conditions $\left(0 \le \frac{T}{rW} \le 2\right)$ and $\left(0.1 \le \frac{z}{r} \le 0.7\right)$ are $(\mu, \sigma) = (0.001, 0.03)$. This means that the expected error in DP estimation is less than 5% (2σ) of the wheel weight. From this result, we can conclude that the suggested estimation method is good for all the terrain types with small error.

3.4 Experimental Validation

A simple equation for DP estimation relating three dimensionless parameters $\frac{DP}{W}$, $\frac{T}{r \cdot W}$ and $\frac{z}{r}$ was developed in Section 3.3. To verify this drawbar-pull estimation method, experiments were done on the FSRL wheel-terrain experimental testbed, which was used for terrain parameter estimation experiments in Chapter 2. Here, the experimental procedure was nearly identical, except that the drawbar-pull was recorded from force/torque sensor readings.

Experiments were performed on two different types of terrain: dry bentonite clay and compacted topsoil. Various slip ratios were applied ranging from 0.2 to 0.8. Figure 3.7 shows the experimental result.

Experimental result on bentonite clay shows a good match to the estimated values. The difference between measured and estimated $\frac{DP}{W}$ is 0.12, which is small considering the range of $\frac{DP}{W}$. The negative estimated value $\frac{DP}{W}$ means that the bentonite clay is a hard-to-traverse medium. In real-world situation, the wheel-terrain interaction can yield negative drawbar-pull on slippery terrain. The negative DP means that terrain exerts a positive resistance force to wheel and the wheel is subject to slow down in horizontal direction.

The estimation value on compacted topsoil shows a deviance from the measured value by about 0.2. Although this difference is not trivial, the estimation result follows the trend of positive and significant DP values (0.15).

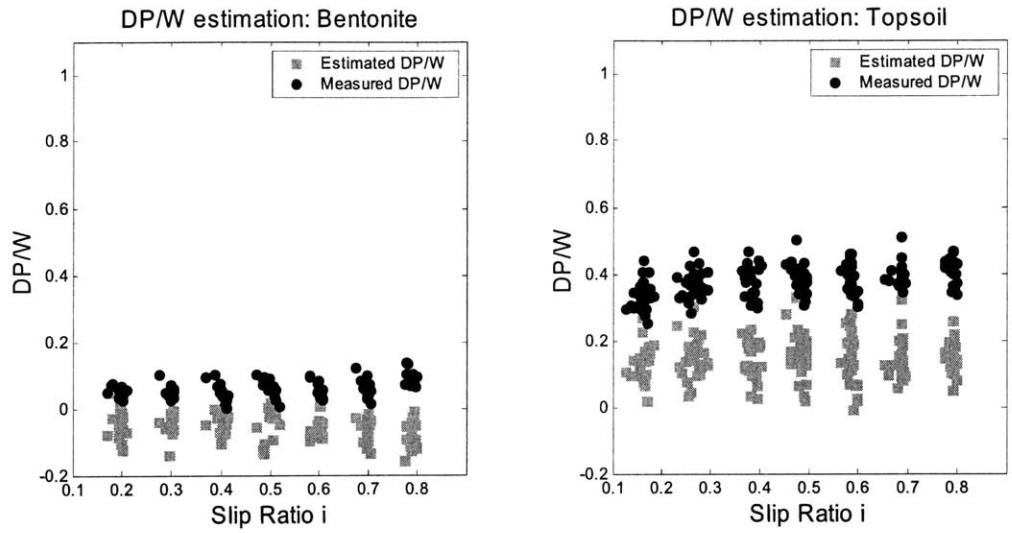

Figure 3.7 Measured and estimated drawbar pull: black O(measured), gray dot(estimated)

Equation 3.21, the estimation equation, came from a least-square plane-fit of simulation data. In experimental environment, there are factors which are not considered in simulation. For example, material transport along the wheel is ignored in simulation. In experiment, if the slip ratio is large, a pile of plowed soil is created behind the wheel and exerts significant amount of DP. Homogeneity of terrain also plays an important role in experiment. Since the medium is not homogeneous, the reaction forces could be different according to the mix of terrain. To take account these unconsidered effects, "experimental correction" on the correction factors $[C_1 \quad C_2 \quad C_3]$ must be performed. A least-square plane-fit was performed using the experimental data on bentonite clay and compacted topsoil. The resulting correction factors are $[1.5 \quad -1 \quad -0.2]$. Estimation result using this "updated" correction factors shows a close match to the experimental data. Difference between measured and estimated DP was 0.04 and the standard deviation of estimation errors is 0.06. This small standard deviation implies that the proposed estimation method follows the general trend of DP generation. To ensure the general usefulness and accuracy, the coefficients C_1, C_2 and C_3 should be determined after

experiments on more extensive types of terrain.

Simulation and theoretical analysis proposed a method to estimate drawbar pull from other simple sensor data. Experimental measurement of actual drawbar pull showed reasonable match with estimated values. Thus it can be concluded that the proposed method is reasonably accurate.

3.5 Traversability Assessment

In sections 3.2~3.4, a method for estimating drawbar-pull was discussed. To assess traversability of terrain from DP, a method for converting DP to traversability must be derived.

In general, DP can be expressed as a function of the slip ratio: $DP = DP(i)$. Figure 3.8 shows the change of DP according to the slip ratio i. Here, we see that drawbar-pull increases as the slip ratio i increases. When i gets larger than a certain value (usually around 0.6, depending on terrain properties), DP reaches a maximum, after which it remains almost constant with increasing i. This value is the maximum drawbar-pull a wheel can generate in a terrain, and can be used as an index of terrain traversability.

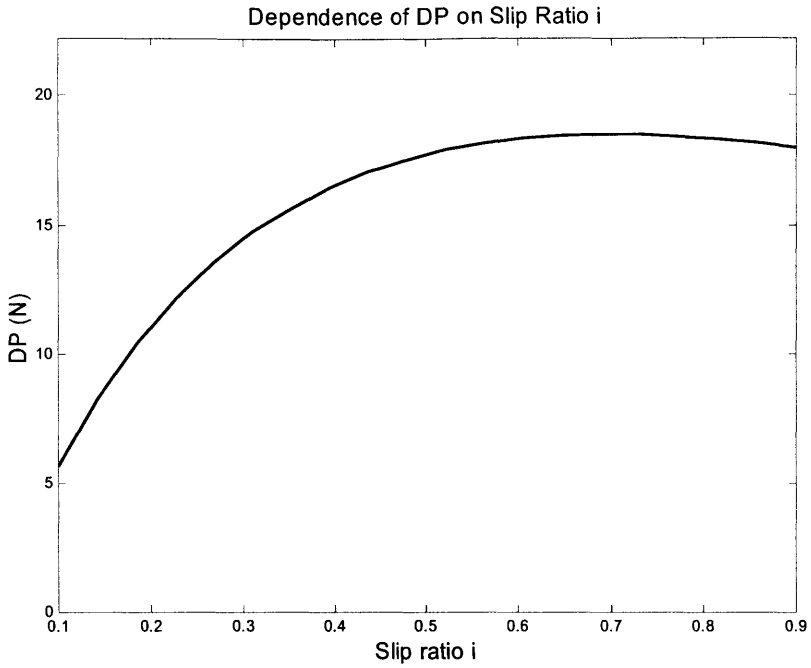

Figure 3.8 DP-*i* relationship on a representative terrain-wheel interaction

It is natural to assign higher traversability to terrains that can exert larger DP. Traversability can be described either in a qualitative or quantitative way. Quantitative methods will assign a numerical metric of traversability. However, since the traversability assessment is based on an estimated DP value, which might have significant error, it may not be appropriate to state traversability quantitatively. A qualitative method of assessing traversability may be more appropriate. One simple way to state the traversability qualitatively is through terrain categorizing. If a terrain can exert DP larger than a preset threshold value, the terrain could be categorized as 'safe' terrain. If a terrain cannot exert a minimum DP, it would be categorized as 'dangerous' terrain. There may be another category called 'marginal' for terrains which can exert DP between the threshold values.

The threshold values can be determined by considering mission objectives or environmental

factors. For example, when a rover is attempting to traverse a hill which has $15°$ inclination, the rover must be able to exert $\frac{DP}{W}$ greater than $\tan(15°)$. In this sense, if the terrain can exert $\frac{DP}{W}$ larger than $\tan(20°)$, it may be categorized as 'safe' terrain. If it can exert $\frac{DP}{W}$ less than $\tan(10°)$, it should be categorized as 'dangerous' terrain. For other cases, it may be categorized as 'marginal' (see Figure 3.9 and 3.10).

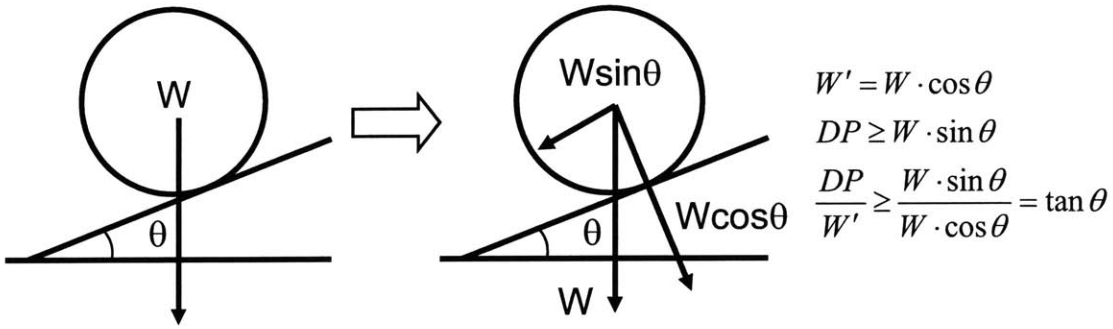

Figure 3.9 Slope and DP threshold setting.
If a wheel is on a ramp, the wheel gets a downward force $W \sin\theta$ and effective weight of $W \cos\theta$. For the wheel to move upward, the wheel should produce a DP larger than the downward force $W \sin\theta$.

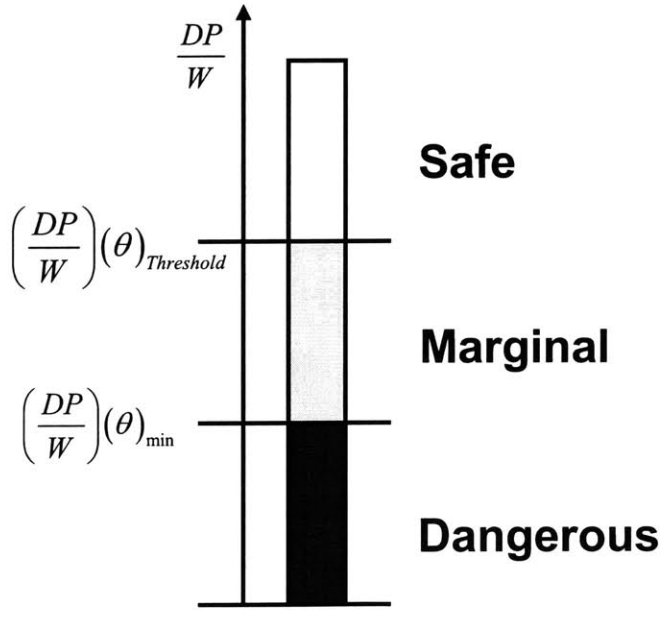

Figure 3.10 DP bar with threshold values indicated.
According to the defined threshold values, traversability of terrain can be defined.

In addition to requirement on $\frac{DP}{W}$, conditions on $\frac{z}{r}$ and $\frac{T}{rW}$ may play important roles in vehicle traversability. For a rover to maintain a clearance distance from the ground, the wheel sinkage must not exceed the distance between the rover bottom and the wheel bottom. In this sense, another criterion on the sinkage can be added to the traversability assessment. If the sinkage exceeds a critical value, which may be close to the vehicle clearance, the terrain a rover is on will be categorized as "dangerous". If the sinkage is lower than a preset threshold value, which is good in terms of ground clearance, the terrain will maintain the category determined by the requirement of DP. If the sinkage of the wheel is between the critical sinkage and the threshold sinkage, since the safety criterion on sinkage is not satisfied, the terrain category determined by DP prediction should be modified one rank lower than its original category (i.e. "safe" to "marginal" and "marginal" to "dangerous"). If there exists requirement on motor torque, similar criterion on traversability assessment can be implemented. Figure 3.13 shows how the traversability of a given terrain is determined:

a) Requirement on drawbar-pull is determined considering mission objectives and terrain environments

b) Safe clearance criterion is added and a "traversability map" is built

c) Drawbar-pull is predicted based on the measurements of the wheel weight, torque, and sinkage

d) Traversability of the terrain is determined by putting the DP and sinkage conditions to the "traversability map"

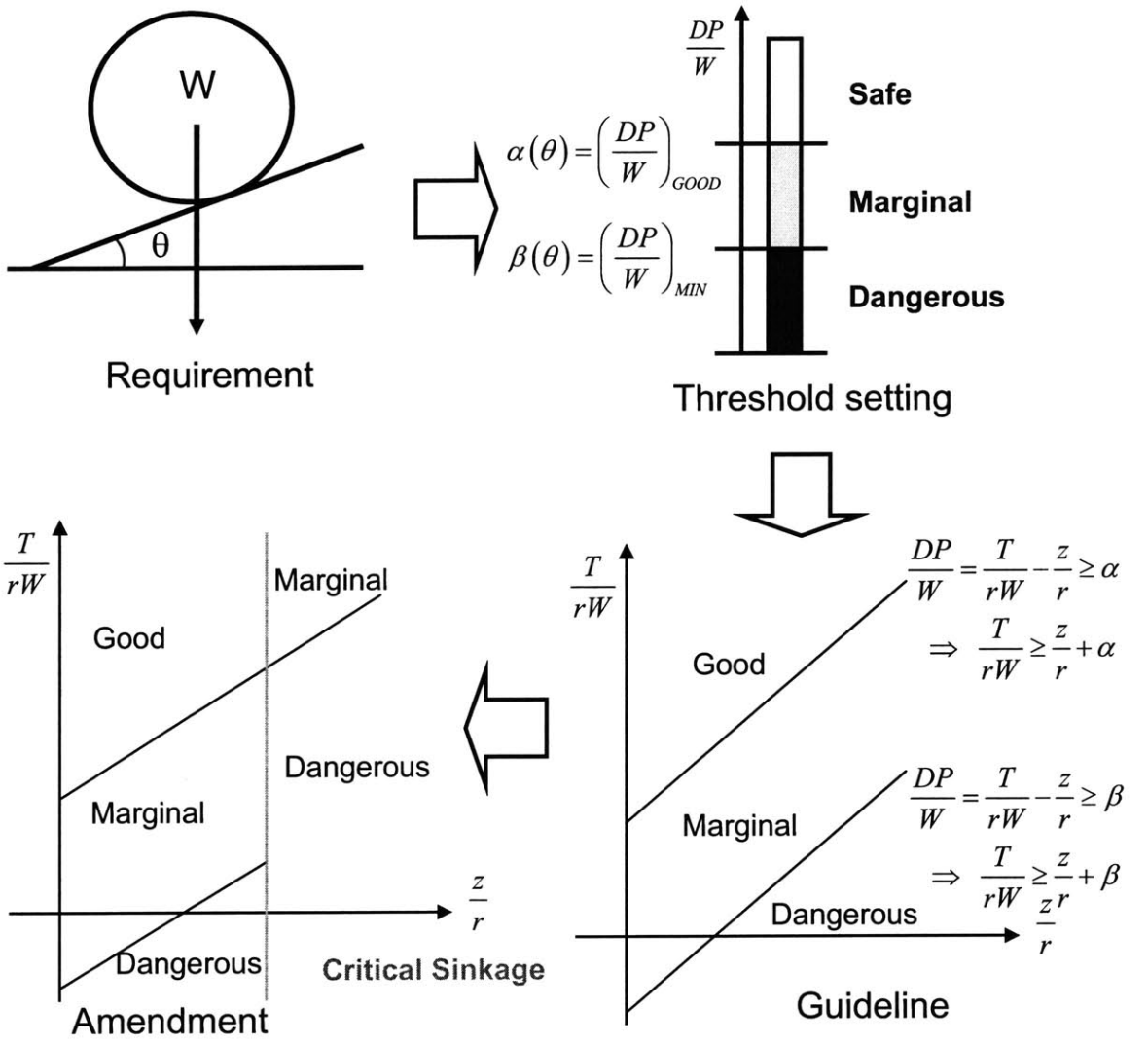

Figure 3.11 Traversability assessment process.

By following these four steps, traversability of terrain can be estimated.

A "traversability map" is built according to a 10° hill- inclination criterion and the clearance requirement on the sinkage to be smaller than 50% of the wheel radius (see Figure 3.12). According to this "traversability map", terrain categorizing on dry bentonite clay and compacted topsoil are performed with the experimental data in Section 3.4. As the $\frac{DP}{W}$ values for each terrain remain almost constant after the slip ratio i exceed 0.4, it is reasonable to use slip ratio i=0.5 as a reference slip ratio for assessing traversability. In general, high slip ratio can result in loss of steerability and control of rover direction on deformable terrain. Since the $\frac{T}{rW}$ and $\frac{z}{r}$ values at slip ratio i = 0.5 on each terrain are (0.1, 0.2) and (0.3, 0.4), dry bentonite clay can be categorized as "dangerous" and compacted topsoil can be categorized as "safe". This result is reasonable considering the loose characteristics of dry bentonite clay, and the firm and cohesive characteristics of compacted topsoil.

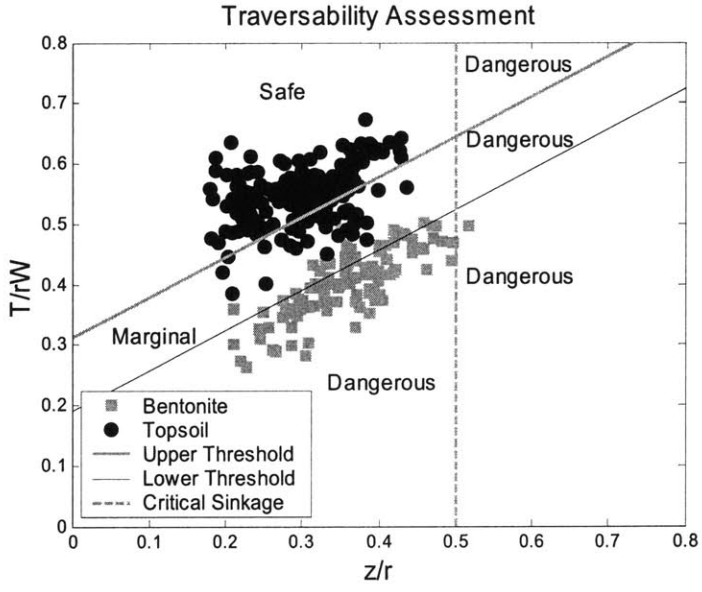

Figure 3.12 Traversabillity assessment on bentonite and topsoil.

According to the traversability assessment steps in Figure 3.11, the traversability of bentonite and topsoil are assessed. Black dots represent z/r and T/rW values of topsoil experiment and gray circles are for bentonite.

In cases at which a rover loses its control on direction, the traversability assessment on DP estimation may not be used. Since the loss of control due to the high slip ratio is beyond the scope of this thesis, it will not be dealt further. However, the relationship between gaining enough DP and losing control on direction must be studied thoroughly complete assessing traversability.

A method of predicting the drawbar-pull a wheel generates on deformable terrain has been developed. This method showed reasonably accurate agreement with measured drawbar-pull values. A method of assessing traversability of terrain based on the predicted drawbar-pull and measured wheel sinkage has been also presented. Since these methods don't need any complicated equipment or rigorous estimation process of other terrain parameters, they are suitable for on-line traversability prediction for planetary exploration rovers.

Chapter 4: Conclusion

4.1 Summary

This thesis described methods for terrain parameter estimation and traversability prediction.

Traditional terrain parameter estimation methods need either special tools or large amount of experimental time. A new linear-offset estimation method was proposed that uses a rover wheel as an experimental tool and doesn't need any special equipment. Due to this simplicity of its equations, this method requires a small amount of computation power, and thus the terrain parameters can be estimated on-line. Both cohesionless and cohesive terrain are suitable for this estimation method.

A traversability assessment method for deformable terrain was also presented. On deformable terrain, soil characteristics play important role in rover mobility and safety. By measuring the sinkage, weight and torque of the wheel, the drawbar-pull can be estimated and the traversability of the terrain can be estimated from the drawbar-pull.

Simulation and experimental results showed that both of these methods can accurately estimate

the terrain parameters and the traversability.

4.2 Contribution of this Thesis

The newly proposed terrain parameter estimation method, the linear-offset method can be used both cohesive and cohesionless terrain. This method is computationally simple and doesn't need any special equipment and long experimental time. Due to the efficiency, this method is suitable for the resource-restricted system such as planetary exploration rovers.

Previous researchers didn't take terrain physical properties such as hardness of terrain into account in rough terrain path planning and failed to describe the mobility of vehicle on deformable terrain. By using the proposed terrain traversability assessment method, terrain information can be associated in path-planning and the safety of rover can be improved.

4.3 Future Works

The proposed estimation method can be used on variety of terrain. To have stable and converging estimation values, the conditioning of data is important. Any help in giving variety of experimental condition such as weight change will increase the performance of estimation method.

The knowledge of terrain deformation modulus K should be known in advance or be estimated during the estimation process. If there comes any noise or disturbance on sensor signals, the estimation of K can show a deviance from true value and lead inaccurate estimation result. A more precise method of deformation modulus K estimation will enhance the performance of c and φ estimation method.

Quasi-static consideration on wheel-terrain interaction is assumed in general. Recent studies on dynamic effect of wheel-terrain interaction addressed that the assumption of quasi-static consideration was not true in practice [25]. Grahn suggested that the linear velocity of a wheel, not the slip ratio i, played an important role in estimating normal and shear stress on wheel-terrain interface [26]. For accurate estimation of terrain parameters, these dynamic effects must be also considered.

In the traversability assessment, interpretation of drawbar-pull to traversabiblity can be greatly changed according to the threshold value of reference drawbar-pull. A standard of terrain conditions would help terrain characterization. Uncertainties from ambiguous standard will be appropriately handled by using fuzzy logic [27, 28].

References

[1] Moore, H.J. and Clow, G.D., "A Summary of Viking Sample-Trench Analyses for Angles of Internal Friction and Cohesions," J. Geophysical Research, vol. 87, No. B12, pp.10,043-10,050, 1982.

[2] Golombek, M.P., "The Mars pathfinder Mission," J. Geophysical Research, vol. 102, No. E2, pp.3,953-3,965, 1997.

[3] Moore, H.J., "Soil-like deposits observed by Sojourner, the Pathfinder rover," J. Geophysical Research, vol. 104, No. E4, pp.8,729-8,746, 1999.

[4] The Rover Team, "The Pathfinder Microrover," J. Geophysical Research, vol. 102, No. E2, pp.3,989-4,001, 1997.

[5] Bekker, M.G., Introduction to terrain-Vehicle Systems, The University of Michigan Press, 1969.

[6] Janosi, Z., and Hanamoto, B., "Analytical Determination of Drawbar Pull as a Function of Slip for Tracked Vehicles in Deformable Soils," Proc. First Int. Conf. On Terrain-Vehicle Systems, 1961.

[7] Wong, J.Y. and Reece, A.R., "Prediction of Rigid Wheel Performance Based on the Analysis of Soil-Wheel Stresses Part 1. Performance of Driven Rigid Wheels," J. Terramechanics, Vol. 4, No. 1, pp.81-98, Pergamon Press, 1967.

[8] McKyes, E. and Ali, O.S., "The Cutting of Soil by Narrow Blades," J. Terramechanics, vol. 14, No. 2, pp.43-58, Pergamon Press, 1977.

[9] Hong, W., Modeling, Estimation, and Control of Robot-Soil Interactions, PhD Thesis, Department of Mechanical Engineering, Massachusetts Institute of Technology, 2001.

[10] Volpe, R., Baumgartner, E., Schenker, P. and Hayati, S., "Technology Development and Testing for Enhanced Mars Rover Sample Return Operations," Proc. 2000 IEEE Aerospace Conference, vol. 7, pp.247-257, 2000.

[11] Kelly, A. and Stentz, A., "Rough Terrain Autonomous Mobility-Part 2: An Active Vision, Predictive Control Approach," Autonomous Robots 5, pp.129-161, Kluwer Academic Publishers, 1998.

[12] Davis, I.L., Kelly, A., Stentz, A. and Matthies, L., "Terrain Typing for Real Robots", Proc. Intelligent Vehicles '95 Symposium, pp.400-405, 1995.

[13] Singh, S., Simmons, R., Smith, T., Stentz, A., Verma, V., Yahji, A. and Schwehr, K., "Recent Progress in Local and Global Traversability for Planetary Rovers," Proc. 2000 IEEE Int'l Conf. on Robotics and Automation, 2000.

[14] Gennery, D., "Traversability Analysis and Path Planning for a Planetary Rover," Autonomous Robots 6, pp.131-146, Kluwer Academic Publishers, 1999.

[15] Howard, A., Seraji, H. and Tunstel, E., "A Rule-Based Fuzzy Traversability Index for Mobile Robot Navigation," Proc. 2001 IEEE Int'l Conf. on Robotics and Automation, 2001.

[16] Iagnemma, K., Genot, F. and Dubowsky, S., "Rapid Physics-Based Rough-Terrain Rover Planning with Sensor and Control Uncertainty," Proc. 1999 IEEE Int'l Conf. on Robotics and Automation, 1999.

[17] Iagnemma, K., Kang, S., Brooks, C., and Dubowsky, S., "Multi-Sensor Terrain Estimation for Planetary Rovers," Proceedings of the Seventh International Symposium on Artificial Intelligence, Robotics and Automation in Space, i-SAIRAS, 2003

[18] Wong, J.Y., Terramechanics and Off-Road Vehicles, ElsevierScience Publishers, 1989.

[19] Yong, R.N., Fattah, E.A. and Skiadas, N., Vehicle Traction Mechanics, Elsevier Science Publishers, 1984.

[20] Wong, J.Y., Theory of Ground Vehicles, John Wiley & Sons, 2001.

[21] Nohse, Y., Hashiguchi, K., Ueno, M., Shikanai, T., Izumi, H. and Koyama, F., "A Measurement of Basic Mechanical Quantities of Off-The-Road Traveling Performance," J. Terramechanics, vol. 28, No. 4, pp.359-370, Pergamon Press, 1991.

[22] Howard, A. and Seraji, H., "Real-Time Assessment of Terrain Traversability for Autonomous Rover Navigation," Proc. 2000 IEEE/RSJ Int'l Conf. on Intelligent Robots and Systems, 2000

[23] Golombek, M. P., Cook, R. A., Economou, T., Folkner, W. M., Haldemann, A. F. C., Kallemeyn, P. H., Knudsen, J. M., Manning, R. M., Moore, H. J., Parker, T. J., Rieder, R., Schofield, J. T., Smith, P. H. and Vaughan, R. M., "Overview of the Mars Pathfinder Mission and Assessment of Landing Site Predictions," Science, vol. 278, pp.1743-1748, 1997.

[24] Lindgren, D. R., Hague, T., Robert Smith, P. J. and Marchant, J. A., "Relating Torque and Slip in an Odometric Model for an Autonomous Agricultural Vehicle," Autonomous Robots, vol. 13, pp73-86, 2002.

[25] Gee-Clough, D., "Soil-Vehicle Interaction (B)," J. Terramechanics, vol. 28, No. 4, pp.289-296, Pergamon Press, 1991.

[26] Grahn, M., "Prediction of Sinkage and Rolling Resistance for Off-The-Road Vehicles Considering Penetration Velocity," J. Terramechanics, vol. 28, No. 4, pp.339-347, Pergamon Press, 1991.

[27] Seraji, H. and Howard, A., "Behavior-Based Robot Navigation on Challenging Terrain: A Fuzzy Logic Approach," IEEE Transactions on Robotics and Automation, vol. 18, No. 3, pp.308-321, 2002.

[28] Ojeda, L. and Borenstein, L., "FLEXnav: Fuzzy Logic Expert Rule-based Position Estimation for Mobile Robots on Rugged Terrain," Proc. 2002 IEEE Int'l Conf. on Robotics and Automation, 2002.

Appendix A: Basic Terramechanics

"Terramechanics" refers to the study of the performance of a machine in relation to its operating environment - the terrain [18]. Although there are well developed semi-empirical theories regarding hard surface-deformable wheel interactions, vehicle performance on deformable terrain remains a largely empirical science. For complete understanding of related researches, basic empirical relationships, which can explain the behavior of deformable terrain, are discussed in this Chapter. Content of this Chapter is mostly a summary of "Terramechanics and Off-Road Vahicles" by Wong [18].

A.1 Pressure–Sinkage Relation

When a vertical force is applied to a plate on deformable terrain, the plate sinks into the terrain (i.e. the terrain deforms) and reaches an equilibrium state. At this equilibrium state, the pressure under the plate due to the vertical force equals the reaction pressure generated by the deformed terrain. The amount of sinkage to reach the equilibrium state for a given vertical pressure is one of the characteristics of terrain. Figure A.1 shows examples of pressure-sinkage relationships. Depending on terrain and the dimension of the plate, the pressure-sinkage relationship exhibits different shapes.

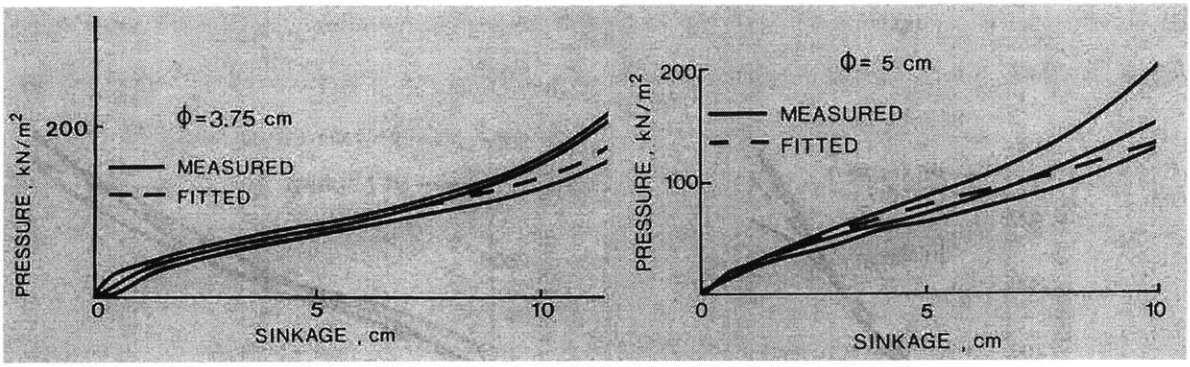

Figure A.1 Pressure-sinkage relation with different tool dimensions on LETE sand ("Terramechanics and Off-Road Vehicle" by J.Y. Wong)

In 1960, Bekker suggested a semi-empirical equation with three terrain parameters K_c, K_φ and n to describe the pressure-sinkage relation of terrain (see Figure A.2) [5]:

$$\sigma = \left(\frac{K_c}{b} + K_\phi \right) z^n \qquad (A.1)$$

where σ is the normal stress on the wheel-terrain interface.

Note that the width of plate "b" is the smaller dimension of the plate.

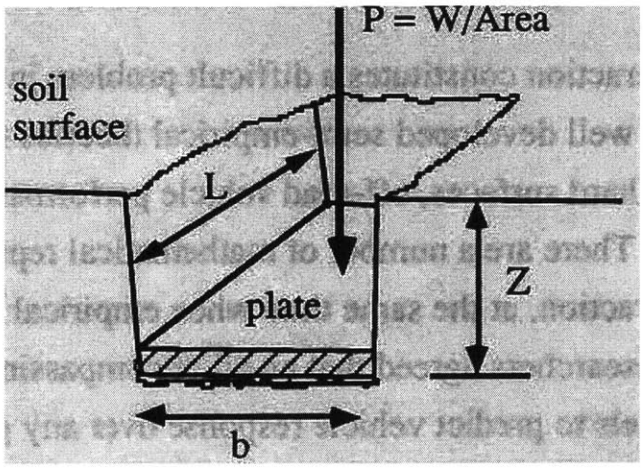

Figure A.2 Plate penetration interaction model ("Dynamics, System and Control Simulation of Planetary Microrover" by C.S. Ma, Master thesis at MIT)

This equation showed good agreement with measured pressure-sinkage relationship and was accepted by many researchers. The three terrain parameters K_c, K_φ and n can be determined by a curve-fitting method on the data from plate penetration experiments with various plate dimensions and vertical pressure conditions. Table A.1 shows published terrain characteristics for several terrain types.

Table A.1 Published terrain characteristics

Terrain type	C	$K_c\left(kN/m^{n+1}\right)$	$K_\phi\left(kN/m^{n+2}\right)$
Sand	1.1	0.95	1523.43
Sandy Loam	0.7	5.27	1515.04
Clayey soil	0.5	13.19	692.15
Heavy clay	0.13	12.7	1555.95
Firm soil	1.2	0.	122788
Medium soil	0.8	29.8	2083

A.2 Normal-Shear Stress Relation

For most deformable terrain types, when shear force is applied, and the shear stress associated with the shear force is larger than a certain value (i.e. the shear strength of the terrain), the terrain fails to retain the force and deforms in the direction of the applied force. If the terrain begins to deform, the shear stress generated by the terrain remains constant [20]. One of the widely used and simplest criterion on the shear strength is the Mohr-Coulomb equation:

$$\tau_{max} = c + \sigma \tan\phi \qquad (A.2)$$

where

τ_{max} : shear strength, σ: normal stress applied to the terrain

c: cohesion of terrain, φ: internal friction angle (frictional constant μ=tanφ)

By assuming an elastic stress-strain relationship before shear stress reaches the shear strength, the stress-strain relation of deformable terrain can be expressed as follows (see Figure A.3):

$$\tau = \tau_{\max} \frac{\varepsilon}{K} \quad for \quad (0 \le \varepsilon \le K), \qquad \tau = \tau_{\max} \quad for \quad (K \le \varepsilon) \tag{A.3}$$

where ε: strain, K: shear deformation modulus

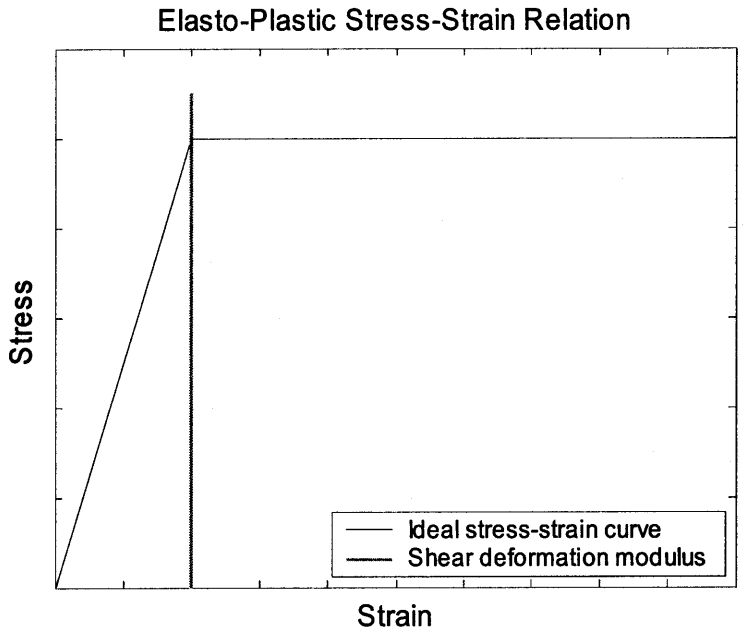

Figure A.3 Idealized elasto-plastic stress-strain relation

Experimental data on deformable terrain shows good agreement with the elasto-plastic model (Figure A.4). However, the sharp transition from elastic to plastic behavior of the elasto-plastic model results in significant deviation from experimental data. To accommodate this deviance, a modified version of Equation (A.3) was proposed by Janosi and Hanamoto [6]:

$$\tau = \tau_{\max}\left(1 - e^{-\frac{j}{K}}\right) = \left(c + \sigma \tan\phi\right)\left(1 - e^{-\frac{j}{K}}\right) \tag{A.4}$$

where

K: shear deformation modulus, j: shear displacement

The shear deformation modulus K may be considered as a measure of the magnitude of the shear displacement that is required to develop the maximum shear stress. The value of K determines the shape of the shear curve. K may be taken as 1/3 of the shear displacement where the shear stress τ is 95% of the maximum shear stress τ_{max} (Figure A.4) [20].

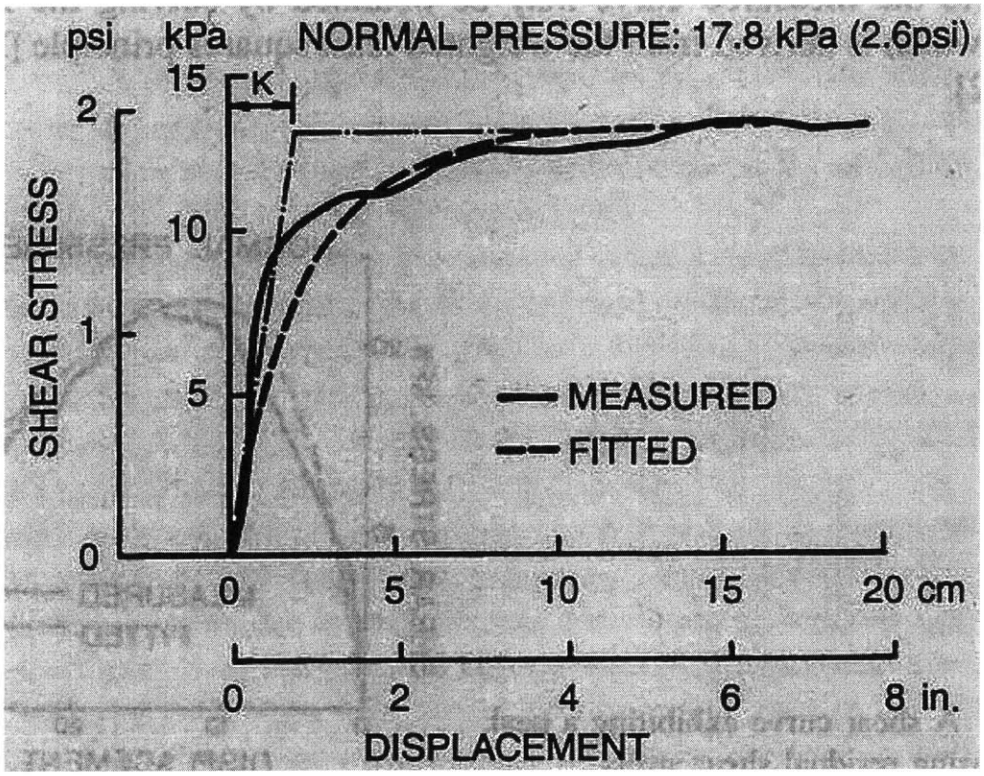

Figure A.4 Measured and estimated shear stress development.
By curve-fitting, all three shear deformation parameters can be estimated.
("Theory of Ground Vehicles" by J.Y. Wong)

Appendix B: Terrain Parameter Estimation Methods

The terrain parameters K_c, K_φ, n, K, c and φ are used to describe the interaction of rigid wheel and deformable terrain. The simplest method of determining these parameters is by using a Bevameter, a specially-designed experimental tool for terrain parameter estimation. Since it is specialized equipment, the Bevameter method could not be used in Martian terrain parameter estimation by the Sojourner rover. Instead, Sojourner used its wheel as experimental tool in the estimation of c and φ. The Sojourner method required long experimental times and off-line estimation. Iagnemma has proposed an on-line estimation method using a wheel as the experimental tool [17]. This Chapter is mostly a summary of "Terramechanics and Off-Road Vahicles" by Wong [18], "Soil-like deposits observed by Sojourner" by Moore [3], and "Multi-Sensor Terrain Estimation for Planetary Rovers" by Iagnemma [17].

B.1 Bevameter Estimation Method

Bekker developed a terrain parameter estimation tool called a Bevameter, consisting of two

major parts: a plate penetration experimental tool, and a shear strength measurement tool (see Figure 1.3). A Bevameter can estimate both terrain pressure-sinkage parameters and shear-strength parameters.

Bekker's pressure-sinkage equation (Equation A.1) incorporates three terrain parameters, K_c, K_φ, and n. Since σ, z and b can be easily measured, Equation (A.1) becomes an equation with three unknown parameters. If more than three sets of experimental data on the pressure-sinkage relation are given, all the three terrain parameters can be estimated by curve-fitting. By applying different normal pressure on several plates with different dimensions, sufficient numbers of data for parameter estimation can be gathered from the plate penetration experiment [19].

Four parameters, τ_{max}, c, φ and K, play important roles in measuring the shear-strength of terrain (Equation A.4). As τ, σ and j are easily measured from the sensors equipped in the Bevameter, Equation A.4 becomes an equation with four unknown values. These four shear-strength parameters can be estimated if more than four sets of experimental data are provided. By applying different normal pressure and measuring associated shear stresses and displacements, sufficient number of data can be gathered [19].

B.2 Sojourner Wheel Spin Estimation Method

The Sojourner rover performed experiments on Mars to estimate terrain shear strength parameters c and φ by using its wheel [3]. The Mohr-Coulomb shear-strength equation (Equation A.2) was used in this estimation method. To estimate c and φ from Equation A.2, more than two sets of normal and shear stress must be measured. During the experiment, Sojourner rotated one of its wheels while others were held fixed. The wheel sinkage into the terrain, wheel torque, and the weight imposed on the fixed wheel were measured/estimated from the wheel motor current, rover camera image of the wheel and track, and the bogie positions [3].

Two assumptions were made on estimating normal and shear stresses from the measurements (see Figure B.1):

a) The wheel torque and weight were uniformly distributed over the wheel-terrain contact area, which was defined as the product of wheel width and the chord corresponding to the wheel sinkage.

b) The developed shear stress was equal to the shear strength of terrain, i.e., the wheel rotational displacement was sufficiently large to develop maximum shear stress.

The normal and shear stresses were estimated as follows:

$$\sigma = \frac{W}{A}, \qquad \tau = \frac{T}{rA}, \qquad A = 2b\sqrt{2rz - z^2} \tag{B.1}$$

where

σ: normal stress, τ: shear stress

W: wheel weight, T: wheel torque, A: contact area

r: wheel radius, b: wheel width, z: sinkage

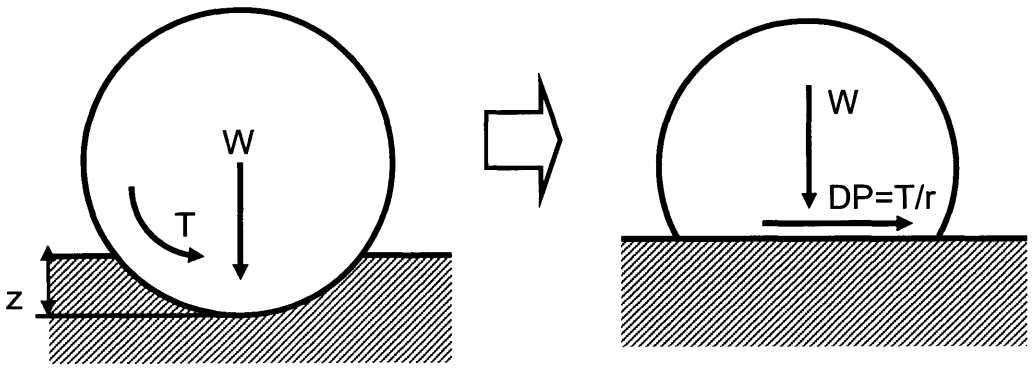

Figure B.1 Force approximation on Sojourner wheel experiment.
W, T, and z can be reproduced as effective weight and DP on effective area A.

By performing experiments with different bogie positions, sufficient weight variation conditions could be achieved. Shear strength parameters c and φ were estimated by putting more than two sets of normal and shear stress values in Equation A.2, and by solving the equations in a least-square fashion.

B.3 Iagnemma's Method

Iagnemma proposed a method for on-line estimation of c and φ using a wheel as the experimental tool (see Figure 2.1 for symbols) [17]. In this method, the normal and shear stress on the wheel-terrain interface were approximated as linear distributions (see Figure 2.2):

$$\begin{aligned} \sigma_1(\theta) &= \frac{\theta_1 - \theta}{\theta_1 - \theta_m}\sigma_m \quad (\theta_m \le \theta \le \theta_1), \qquad \sigma_2(\theta) = \frac{\theta}{\theta_m}\sigma_m \quad (0 \le \theta \le \theta_m) \\ \tau_1(\theta) &= \frac{\theta_1 - \theta}{\theta_1 - \theta_m}\tau_m \quad (\theta_m \le \theta \le \theta_1), \qquad \tau_2(\theta) = \frac{\theta}{\theta_m}\tau_m \quad (0 \le \theta \le \theta_m) \end{aligned} \tag{B.2}$$

Wong proposed a method to estimate the location of the maximum normal stress, θ_m [7]. In general, θ_m can be estimated if two terrain parameters c_1 and c_2, slip ratio *i*, and the sinkage angle θ_1 are known;

$$\theta_m = (c_1 + ic_2)\theta_1 \tag{B.3}$$

The range of parameters c_1 and c_2 is generally $c_1 \cong 0.4$ and $0 \le c_2 \le 0.3$. For a wide range of slip ratios, the range of $(c_1 + ic_2)$ will be around 0.5 ($0.4 \le (c_1 + ic_2) \le 0.6$). Thus, without loss of generality, θ_m can be approximated as $\theta_m = \frac{\theta_1}{2}$. With this approximation, the wheel weight and torque can be calculated and the associated maximum normal and shear stress σ_m and τ_m can be estimated as follows:

$$\begin{aligned} T &= \int \tau \cdot dA \\ &= r^2 b\left(\int_{\theta_m}^{\theta_1} \tau_1(\theta) \cdot d\theta + \int_0^{\theta_m} \tau_2(\theta) \cdot d\theta \right) \\ &= \frac{r^2 b \theta_1}{2}\tau_m \end{aligned} \tag{B.4}$$

$$
\begin{aligned}
W &= \int (\sigma\cos\theta + \tau\sin\theta)\cdot dA \\
&= rb\left(\begin{array}{l}\int_{\theta_m}^{\theta_1}\sigma_1(\theta)\cos\theta\cdot d\theta + \int_0^{\theta_m}\sigma_2(\theta)\cos\theta\cdot d\theta \\ +\int_{\theta_m}^{\theta_1}\tau_1(\theta)\sin\theta\cdot d\theta + \int_0^{\theta_m}\tau_2(\theta)\sin\theta\cdot d\theta\end{array}\right) \\
&= \frac{2br}{\theta_1}\left(\left(2\cos\frac{\theta_1}{2}-\cos\theta_1-1\right)\sigma_m + \left(2\sin\frac{\theta_1}{2}-\sin\theta_1\right)\tau_m\right)
\end{aligned}
\tag{B.5}
$$

From B.4 ad B.5,

$$
\tau_m = \frac{2T}{r^2 b\theta_1} \tag{B.6}
$$

$$
\begin{aligned}
\sigma_m &= \frac{\frac{\theta_1}{2rb}W - \left(2\sin\frac{\theta_1}{2}-\sin\theta_1\right)\tau_{\max}}{2\cos\frac{\theta_1}{2}-\cos\theta_1-1} \\
&= \frac{\frac{\theta_1}{2rb}W - \left(2\sin\frac{\theta_1}{2}-\sin\theta_1\right)\frac{2}{r^2 b\theta_1}T}{2\cos\frac{\theta_1}{2}-\cos\theta_1-1}
\end{aligned}
\tag{B.7}
$$

By substituting Equations B.6 and B.7 into the normal-shear stress relation (Equation 2.6), one equation relating W, T, z and i to c and φ can be obtained:

$$
c + \frac{\left(\frac{W}{rb} - \left(2\sin\frac{\theta_1}{2}-\sin\theta_1\right)\frac{4T}{\theta_1^2 r^2 b}\right)}{\frac{2}{\theta_1}\left(2\cos\frac{\theta_1}{2}-\cos\theta_1-1\right)}\cdot\tan\phi = \frac{2T}{\theta_1 r^2 b\left(1-e^{-\frac{r}{K}\left(\frac{\theta_1}{2}-(1-i)\left(\sin\theta_1-\sin\frac{\theta_1}{2}\right)\right)}\right)} \tag{B.8}
$$

Four parameters in Equation B.8, (W, T, θ_1 and i), can be measured from sensors on the wheel. The shear deformation modulus K can be estimated from a method suggested in Appendix D of this thesis, or can be chosen as a representative value for deformable terrain [17]. By putting

these values into Equation B.8, a single equation in two unknown parameters, c and φ, can be obtained.

Several sets of data for W, T, θ_1 and *i* are measured during the estimation process. If j sets of data are collected, Equation B.8 can be written j times, and this equations can be solved in a least square fashion:

$$K_1 \cdot \begin{bmatrix} c \\ \tan\phi \end{bmatrix} = K_2 \tag{B.9}$$

$$\begin{bmatrix} c \\ \tan\phi \end{bmatrix} = \left(K_1{}^T K_1\right) \cdot K_1{}^T K_2 \tag{B.10}$$

where

$$K_1 = \begin{bmatrix} 1 & K_{11} \\ 1 & K_{21} \\ \vdots & \vdots \\ 1 & K_{j1} \end{bmatrix}, \qquad K_{j1} = \frac{\left(\frac{W}{rb} - \left(2\sin\frac{\theta_1}{2} - \sin\theta_1\right)\frac{4T}{\theta_1{}^2 r^2 b}\right)}{\frac{2}{\theta_1}\left(2\cos\frac{\theta_1}{2} - \cos\theta_1 - 1\right)} \tag{B.11}$$

and

$$K_2 = \begin{bmatrix} K_{12} \\ K_{22} \\ \vdots \\ K_{j2} \end{bmatrix}, \qquad K_{j2} = \frac{2T}{\theta_1 r^2 b\left(1 - e^{-\frac{r}{K}\left(\frac{\theta_1}{2} - (1-i)\left(\sin\theta_1 - \sin\frac{\theta_1}{2}\right)\right)}\right)} \tag{B.12}$$

Simulation results on this method showed a good match to the true values on low and moderate cohesive terrains.

Appendix C: Wheel-Terrain Interaction Models

Since many man-made vehicles use wheels as actuators, the mechanism of wheel-terrain interaction has been a great interest to researchers. Wheel-terrain interactions can be classified as one of four cases:

a) Rigid wheel-rigid terrain
b) Rigid wheel-deformable terrain
c) Deformable wheel-rigid terrain
d) Deformable wheel-deformable terrain

Among these four cases, the rigid wheel-deformable terrain situation is the most interesting, since most planetary exploration rovers use rigid wheels, and in many cases pneumatic tires can also be regarded as rigid wheels if the terrain is soft [20]. This Chapter is mostly a summary of "Terramechanics and Off-Road Vahicles" by Wong [18].

C.1 Rigid Wheel-Deformable Terrain Interaction Model

Bekker suggested that the pressure-sinkage relation in wheel-terrain interaction could be well described by Equation A.1. However, experimental measurement of the actual normal stress distribution showed significant deviance from the estimated normal stress distribution by Equation C.1 (see Figure C.1) [20, 21].

$$\begin{aligned}\sigma(\theta) &= \left(\frac{k_c}{b}+k_\phi\right) z(\theta)^n \\ &= \left(\frac{k_c}{b}+k_\phi\right)\left(r\cos\theta - r\cos\theta_1\right)^n \\ &= \left(\frac{k_c}{b}+k_\phi\right) r^n\left(\cos\theta - \cos\theta_1\right)^n\end{aligned} \tag{C.1}$$

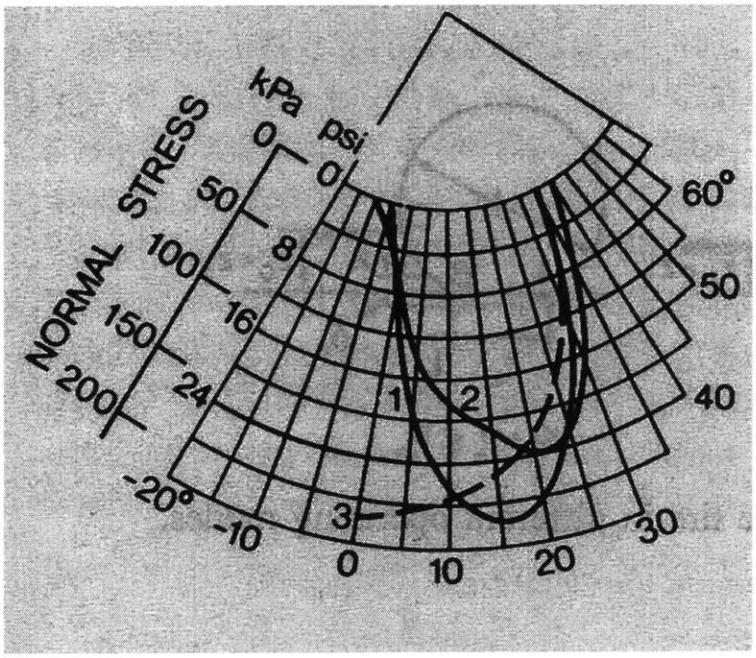

Figure C.1 Normal stress distribution on wheel-terrain interface.

Bekker's approximation (dashed line) show deviance from the measured distributions (solid lines) on one end of wheel-terrain interface.

("Theory of Ground Vehicles" by J.Y. Wong)

In general, the normal and shear stress distributions show peak values around the center of the wheel-terrain interface (i.e. at $\theta = \frac{\theta_1}{2}$). To take this tendency into account, Wong proposed a method of estimating normal stress between a driven wheel and deformable terrain [7]. In Wong's wheel-terrain interaction model, two more terrain parameters c_1 and c_2 are introduced (see Figure 2.1 for symbols):

$$\theta_m = \theta_1(c_1 + c_2 i) \qquad (C.2)$$

where

θ_m : contacting angle at which peak normal stress occurs

In the front region (where the contacting angle is larger than θ_m), the normal stress can be estimated with Equation C.1. In the rear region (other than the front region), the normal stress distribution is assumed to be symmetrical. The normal stress distribution in rear region can be estimated by using this symmetry (see Figure C.2).

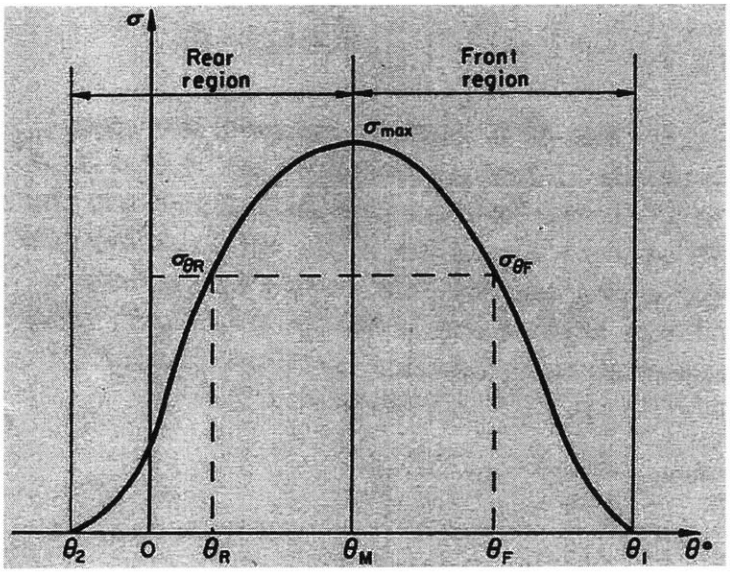

Figure C.2 Symmetric normal stress distribution.

By using this symmetry, normal stress in the rear region can be estimated. $\sigma_{\theta F}$ and $\sigma_{\theta R}$ refer to the normal stress developed in the front and rear region. These are often written as σ_1 and σ_2.

("Prediction of Rigid Wheel Performance Based on the Analysis of Soil-Wheel Stresses Part 1" by J.Y. Wong and A.R. Reece)

$$\frac{\theta_R-\theta_2}{\theta_m-\theta_2}=\frac{\theta_1-\theta_F}{\theta_1-\theta_m}\ \Rightarrow\ \theta_F=\frac{(\theta_1-\theta_2)\theta_m}{\theta_m-\theta_2}-\frac{(\theta_1-\theta_m)\theta_R}{\theta_m-\theta_2}\ \Rightarrow\ \sigma_{0R}=\sigma_{0F} \tag{C.3}$$

where θ_F, θ_R, σ_F and σ_R refer to the contacting angle and associated normal stress in front and rear region. σ_F and σ_R can be substituted with σ_1 and σ_2:

$$\sigma_1(\theta)=\left(\frac{K_c}{b}+K_\varphi\right)r^n(\cos\theta-\cos\theta_1)^n \tag{C.4}$$

By substituting Equation C.3 into Equation C.4, σ_2 can be estimated as:

$$\sigma_2(\theta)=\left(\frac{K_c}{b}+K_\phi\right)r^n\left(\cos\left(\frac{(\theta_1-\theta_2)\theta_m}{\theta_m-\theta_2}-\frac{(\theta_1-\theta_m)\theta}{\theta_m-\theta_2}\right)-\cos\theta_1\right)^n \tag{C.5}$$

Figure C.3 shows the comparison of measured and estimated normal (radial) stress distribution. Wong's estimation method is considered sufficiently accurate for many researchers [7].

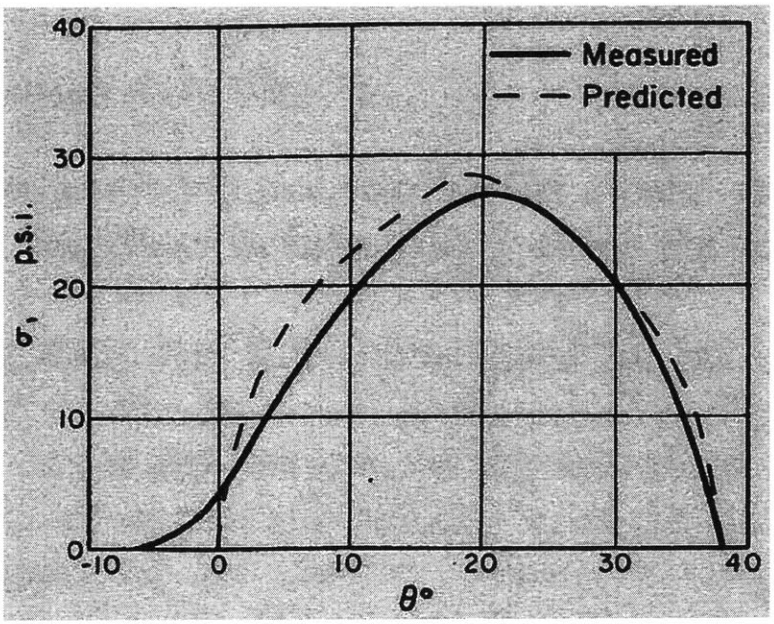

Figure C.3 Measured and estimated normal stress distribution.
Wong's method shows good agreement with experimental measurement.
("Terramechanics and Off-Road Vehicles" by J.Y. Wong)

Shear stress at the wheel-terrain interface can be calculated using Equation A.4. The shear displacement j of the wheel-terrain interface is a function of wheel slip ratio and contacting angle. The shear stress associated with the normal stress can be expressed as follows [7]:

$$\mathrm{j}(\theta) = r\left((\theta_1 - \theta) - (1-\mathrm{i})(\sin\theta_1 - \sin\theta)\right) \tag{C.6}$$

$$\tau(\theta) = \left(c + \sigma(\theta)\tan\phi\right)\left(1 - e^{-\frac{\mathrm{j}}{K}}\right) = \left(c + \sigma(\theta)\tan\phi\right)\left(1 - e^{-\frac{r}{K}((\theta_1-\theta)-(1-\mathrm{i})(\sin\theta_1-\sin\theta))}\right) \tag{C.7}$$

Note that this relation can be used both in front and rear regions.

Comparison between estimated and measured stress distributions are made in Figure C.4. It can be seen that the proposed approximation method can closely follow the actual stress distribution and can be concluded that this method is sufficiently accurate.

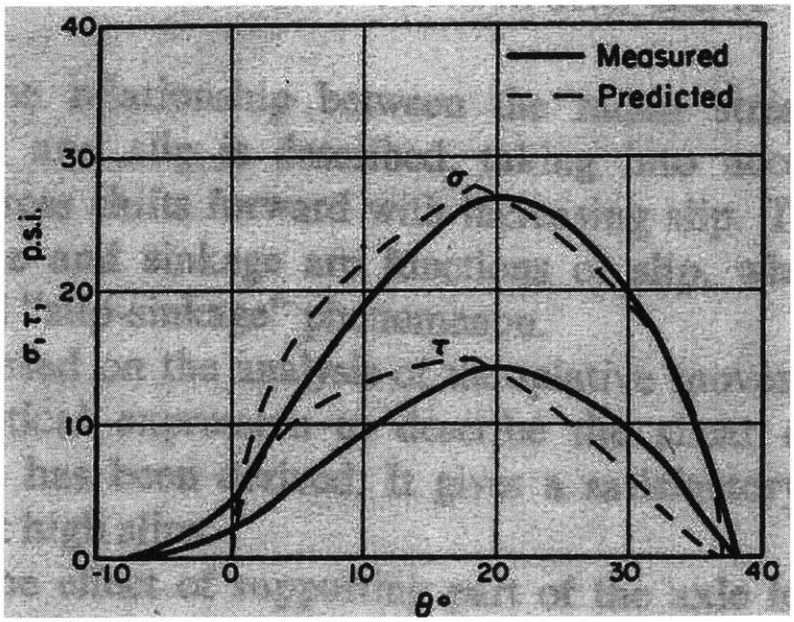

Figure C.4 Measured and estimated normal and shear stress distributions.
Shear stress estimated with Equation C.7 shows a good match to experimental measurement.
("Terramechanics and Off-Road Vehicles" by J.Y. Wong)

Wheel-terrain interaction forces and sinkage can be uniquely determined from the estimated stress distribution. If the sinkage z (hence the contacting angle θ_1) and slip ratio i are known, the reaction forces W, DP and T can be computed as follows:

$$\begin{aligned} W &= \int (\sigma \cos\theta + \tau \sin\theta) \cdot dA \\ &= rb\left[\left(\int_{\theta_m}^{\theta_1} \sigma_1 \cos\theta \cdot d\theta + \int_0^{\theta_m} \sigma_2 \cos\theta \cdot d\theta\right) + \left(\int_{\theta_m}^{\theta_1} \tau_1 \sin\theta \cdot d\theta + \int_0^{\theta_m} \tau_2 \sin\theta \cdot d\theta\right)\right] \end{aligned} \tag{C.8}$$

$$T = \int r\tau \cdot dA = r^2 b\left(\int_{\theta_m}^{\theta_1} \tau_1 \cdot d\theta + \int_0^{\theta_m} \tau_2 \cdot d\theta\right) \tag{C.9}$$

$$\begin{aligned} DP &= \int (\tau \cos\theta - \sigma \sin\theta) \cdot dA \\ &= rb\left[\left(\int_{\theta_m}^{\theta_1} \tau_1 \cos\theta \cdot d\theta + \int_0^{\theta_m} \tau_2 \cos\theta \cdot d\theta\right) - \left(\int_{\theta_m}^{\theta_1} \sigma_1 \sin\theta \cdot d\theta + \int_0^{\theta_m} \sigma_2 \sin\theta \cdot d\theta\right)\right] \end{aligned} \tag{C.10}$$

Sinkage z can be determined by trial-and-error fashion. A reasonable amount of sinkage is first assumed and all the reaction forces are computed using Equations C.8~C.10. If the upward reaction force W is larger than the weight of the wheel, then the assumed sinkage is larger than the actual value. If W is smaller than the weight, then the sinkage should be larger than the assumed one. A few trials can yield a sufficiently accurate value of sinkage. If the sinkage is determined, the computation of other reaction forces are straightforward.

C.2 Other Wheel-Terrain Interaction Models

Three more wheel-terrain interaction models are proposed and widely accepted by many researchers. However, the scope of this thesis is rigid wheel-deformable terrain interaction, only a brief review on other models will be given.

C.2.1 Rigid Wheel-Rigid Terrain Interaction

Rigid wheel-rigid terrain interaction can be modeled as two objects contacting each other. Since both the wheel and the terrain are rigid, the contacting area is only a point (or line for 3D case), normal and shear stress cannot be calculated. If terrain is flat, normal reaction force from the terrain is equal to the weight of the wheel and the shear force can be calculated by Coulomb's law of friction:

$$\begin{aligned} DP &= \frac{T}{r} \qquad \left(\frac{T}{r} \le \mu_s W \quad and \quad wheel \quad doesn't \quad slip\right) \\ DP &= \mu_k W \qquad \left(wheel \quad slips\right) \end{aligned} \tag{C.11}$$

C.2.2 Deformable Wheel (Pneumatic Tire)-Rigid Terrain Interaction

When terrain is rigid and the wheel (tire) is deformable, the tire deforms until the normal reaction force from the tire air pressure and carcass stiffness reaches its weight and makes equilibrium. In computing the shear stress distribution on the deformed wheel-terrain interface, the elasticity of tire must be considered. Motion resistance can be occurred due to the hysteresis of tire and air.

C.2.3 Deformable Wheel-Deformable Terrain Interaction

Deformable wheel-deformable terrain interaction is similar to that of deformable wheel-rigid terrain. The tire deforms until the normal reaction forces reaches the weight of the wheel. The deformed wheel sinks into the terrain until the earth pressure reaches equilibrium with the pressure from the air in the tire and carcass stiffness. Shear stress on the wheel-terrain interface can be computed by using Equation A.4.

Four types of wheel-terrain interaction model were briefly discussed. Rigid wheel-deformable terrain interaction model is of most interest since planetary exploration rovers generally use rigid wheel, and even pneumatic tires can be regarded as rigid wheel on soft terrain.

Appendix D: Shear Deformation Modulus Estimation

In terrain parameter estimation methods which use wheels as experimental tools, the shear deformation modulus K plays an important role. For the methods proposed by Iagnemma [10] and the one developed in Chapter 2, reasonably accurate values of K is indispensable. Traditional estimation methods of K involve special equipment such as a Bevameter. Since it is not practical for planetary rovers to have a dedicated tool for K estimation, an alternative method is needed.

D.1 Estimation by Error Minimization

In Chapter 2, it is shown that the proposed wheel-terrain interaction relationship, Equations 2.11 and 2.12, are sufficiently accurate. If the shear deformation modulus K_e used in estimation is sufficiently accurate (close to the true K), it is expected that the estimation result of c and φ are also accurate. Accurate estimation result implies that the estimation parameters (M_3, M_4) lie close to the curve describing the true parameters (see Figure 2.7). Figure D.1 shows the actual parameter curve and estimated parameter points for different K_e values.

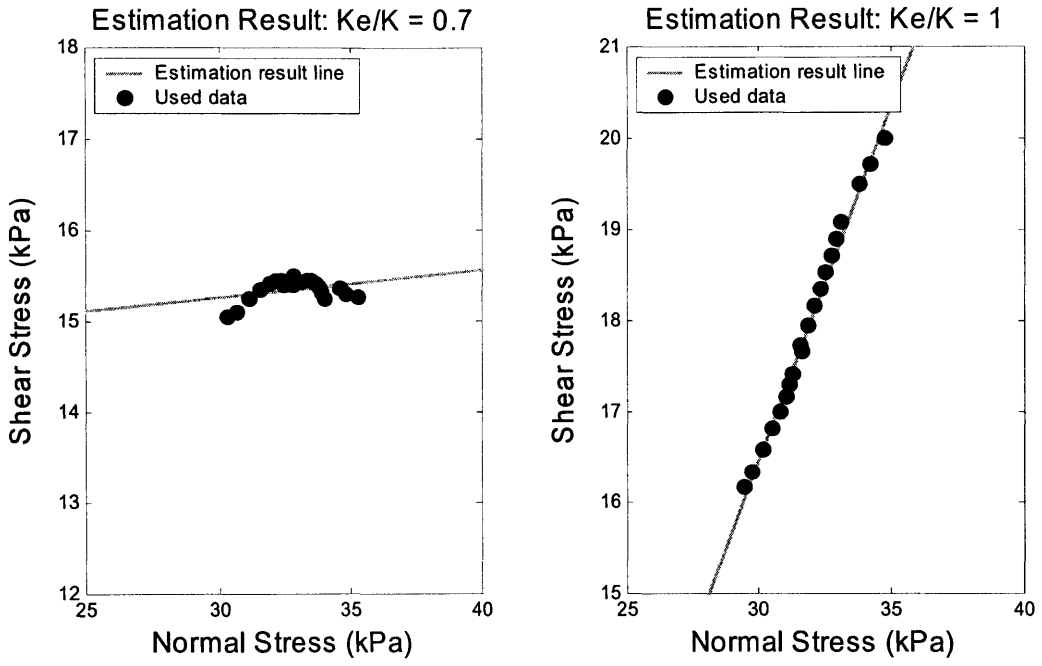

Figure D.1 Estimation error associated with K_e

It is reasonable to assume that the data points lie close to the result curve when the estimated K_e is close to the true K. Error between the actual parameter curve and estimated data points can be defined as follow:

$$Err(K_e) = \sum err_i \tag{D.2}$$

where

err_i : distance between result curve $y = x \tan\varphi + c$ and i'th data point

K_e : shear deformation modulus used in the estimation

Note that $Err(K_e)$ is not the amount of error on K_e. Rather, it is more a penalty for estimating inaccurate K_e. If the trial value of K_e is close to the real K, then the associated $Err(K_e)$ will be small. If the trial value of K_e is much different to the real K, then the

associated $Err(K_e)$ will be large. Figure D.2 shows the tendency of the estimation error $Err(K_e)$ on a representative terrain type and wheel operating conditions. It can be seen that the error approaches its minimal value as K_e approaches to the true shear deformation value. This implies that the shear deformation modulus K can be reasonably estimated by minimizing the associated estimation error $Err(K_e)$.

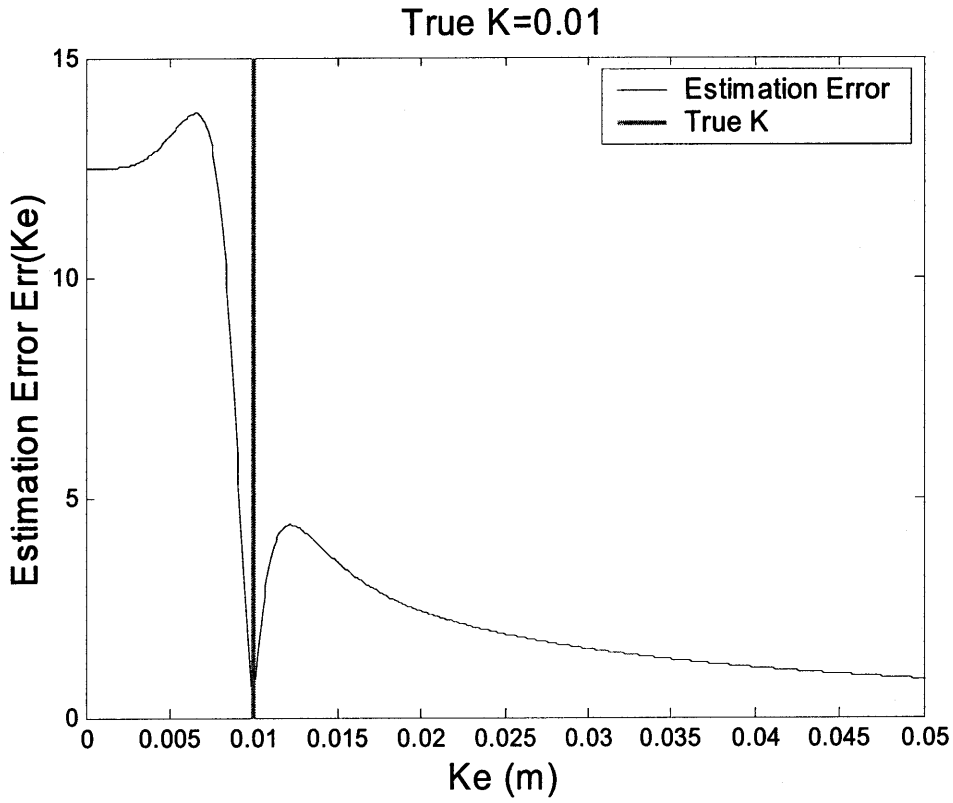

Figure D.2 Estimation Error associated with K_e.
By Minimizing this Err(Ke), a reasonably accurate K_e can be estimated.

By computing $Err(K_e)$ and finding K_e which involves the smallest $Err(K_e)$, the value of shear deformation modulus K can be estimated with sufficient accuracy.

D.2 Estimation by Effective Torque

In the terrain parameter estimation process, shear deformation modulus K is used in the computation of "correction factors" A and B in Equation 2.8. If the values of A and B are known, the value of K can be estimated from Equations 2.7.

In Appendix C, it is shown that $\theta_m = \frac{\theta_1}{2}$ in general. By using this approximation, the wheel torque T in Equation 2.2 can be rewritten as follow:

$$T = r^2 b\theta_1 \left(\frac{\sigma_m \tan\phi}{2} A + \frac{c}{2}\left(A + \frac{B}{2} \right) \right) \tag{D.3}$$

B is the ratio of shear stress developed at the bottom of the wheel-terrain interface to its maximum value (Equation 2.8). B tends to approach to 1 as the wheel radius is large, deformation modulus K is small, and slip ratio *i* is large. Considering the usual range of wheel radius r and deformation modulus K, it is reasonable to approximate B as 1 on most slip ratio and wheel sinkage values. For moderate slip ratio *i*, Equation D.3 can thus be rewritten as follow:

$$T = \left(\frac{\sigma_m \tan\phi}{2} A + \frac{c}{2} A + \frac{c}{4} \right) r^2 b\theta_1 \tag{D.4}$$

A is the ratio of shear stress developed at the center of wheel-terrain interface to the maximum shear stress which can be developed at $\theta_m = \frac{\theta_1}{2}$. When the slip ratio *i* is large, the shear stress developed at the center of the wheel terrain interface is close to its maximum, and A becomes 1. In this case, the associated maximum wheel torque T_m can be expressed follow:

$$T_m = r^2 b\theta_1 \left(\frac{\sigma_m \tan\phi}{2} + \frac{c}{2}\left(1 + \frac{1}{2} \right) \right) = r^2 b\theta_1 \left(\frac{\sigma_m \tan\phi}{2} + \frac{3c}{4} \right) \tag{D.5}$$

For most soil types, there is material transport along the wheel-terrain interface due to wheel movement. In this case, the wheel sinkage does not vary much as the slip ratio *i* changes. Figure E.4 shows the change of sinkage against slip ratio *i* on a representative terrain. Without loss of generality, it is reasonable to say that if the weight of a wheel is fixed, the sinkage (hence the contacting angle θ_1) can be considered constant.

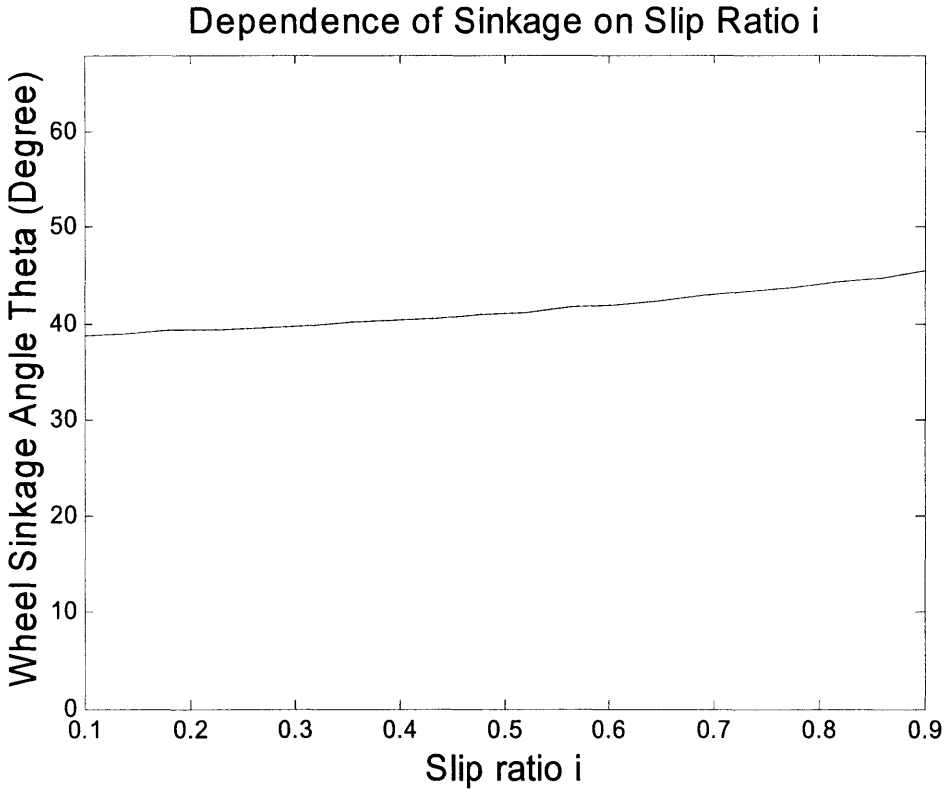

Figure D.3 Dependence of sinkage on slip ratio *i*.
Sinkage doesn't change significantly as slip ratio *i* changes. Thus the sinkage can be considered as constant.

By assuming that θ_1 is constant for moderate-large slip ratios, it is reasonable to assume that the θ_1, and thus σ_m (since σ_m is a function of θ_1) in Equations D.4 and D.5 are the same. The ratio of T and T_m can be expressed as follow:

$$\frac{T}{T_m}=\frac{\left(\frac{\sigma_m \tan\phi}{2}A+\frac{c}{2}A+\frac{c}{4}\right)r^2 b\theta_1}{\left(\frac{\sigma_m \tan\phi}{2}+\frac{3c}{4}\right)r^2 b\theta_1}=\frac{\left(\frac{\sigma_m \tan\phi}{2}+\frac{3c}{4}\right)A-\frac{c}{4}A+\frac{c}{4}}{\frac{\sigma_m \tan\phi}{2}+\frac{3c}{4}} \qquad (D.6)$$

$$=A+\frac{c}{(3c+2\sigma_m \tan\phi)}(1-A)$$

In general, the maximum normal stress σ_m is much greater than the cohesion c. Since the range of A is $0 \le A \le 1$, the range of (1-A) is also $0 \le (1-A) \le 1$, and the order of these two terms are equal. In this sense, the second term in Equation D.6, $\frac{c}{(3c+2\sigma_m \tan\varphi)}(1-A)$, can be considered much smaller than the first term, A. With reasonable accuracy, Equation D.6 can be rewritten with omitting the second term, $\frac{c}{(3c+2\sigma_m \tan\varphi)}(1-A)$:

$$\frac{T}{T_m} \cong A \qquad (D.7)$$

The maximum torque T_m can be estimated by applying a high slip ratio *i*. If T_m is obtained, the "correction factors" A and B can be estimated by Equation D.7 for A, and setting B equal to 1.

Once the value of A is known, shear deformation modulus K can be calculated as follow (refer to Equation 2.7):

$$K=-\frac{r\left(\frac{\theta_1}{2}-(1-i)\left(\sin\theta_1-\sin\frac{\theta_1}{2}\right)\right)}{\ln(1-A)} \qquad (D.8)$$